Structural and Multidisciplinary Optimization (2019) 59:461–483
https://doi.org/10.1007/s00158-018-2076-2

RESEARCH PAPER

Design of periodic elastoplastic energy dissipating microstructures

Ryan Alberdi[1] · **Kapil Khandelwal**[1]

Received: 7 March 2018 / Revised: 6 August 2018 / Accepted: 19 August 2018 / Published online: 6 September 2018

Abstract

The design of periodic elastoplastic microstructures for maximum energy dissipation is carried out using topology optimization. While the topology optimization of elastic microstructures has been performed in numerous studies, microstructural design considering inelastic behavior is relatively untouched due to a number of reasons which are addressed in this study. An RVE-based multiscale model is employed for computational homogenization with periodic boundary constraints, satisfying the Hill-Mandel principle. The plastic anisotropy which may be prevalent in materials fabricated through additive manufacturing processes is considered by modeling the constitutive behavior at the microscale with Hoffman plasticity. Discretization is done using enhanced assumed strain elements to avoid locking from incompressible plastic flow under plane strain conditions and a Lagrange multiplier approach is used to enforce periodic boundary constraints in the discrete system. The design problem is formulated using a density-based parameterization in conjunction with a SIMP-like material interpolation scheme. Attention is devoted to issues such as dependence on initial design and enforcement of microstructural connectivity, and a number of optimized microstructural designs are obtained under different prescribed deformation modes.

Keywords Architectured microstructures · Nonlinear topology optimization · RVE-based multiscale models · Computational homogenization · Anisotropic plasticity

1 Introduction

The properties of materials employed for engineering purposes have an inherent dependence on their heterogeneous composition. Indeed, at a certain scale, all materials have heterogeneities which affect their engineering properties at the scale of application. Recently, new classes of materials known as architectured materials and mechanical metamaterials have emerged in large part due to the rapid development of additive manufacturing technologies which allow improved feature control at smaller scales (Guo and Leu 2013; Xu et al. 2015; Li et al. 2016). These materials derive their properties through purposeful design of the geometry and composition of microstructures (Fleck et al. 2010; Lee et al. 2012; Christensen et al. 2015). One of the most successful numerical design tools in computational mechanics is topology optimization, which is used to determine the optimal layout of a limited amount of material within a design domain in order to achieve the best design performance (Bendsøe and Sigmund 2003). This allows for the simultaneous optimization of size, shape, and connectivity and has seen topology optimization successfully employed in a variety of design problems, including the design of material microstructures (Cadman et al. 2013). An important property for which material microstructures can been designed is that of energy dissipation. For instance, metallic foams are widely used to dissipate energy through plastic deformations (Lefebvre et al. 2008). More recently, architectured materials such as metallic micro-lattices have been shown to be superior to metallic foams in their ability to dissipate energy (Schaedler et al. 2014; Rashed et al. 2016). However, the application of topology optimization to the design of material microstructures for energy dissipation is a topic which has been largely unexplored, due

Responsible Editor: Jianbin Du

✉ Kapil Khandelwal
kapil.khandelwal@nd.edu

[1] Department of Civil, Environmental Engineering, Earth Sciences University of Notre Dame, 156 Fitzpatrick Hall, Notre Dame, IN 46556, USA

to the difficulties inherent in forward and inverse problems involving multiscale inelastic behavior.

Early works considering material microstructural design through topology optimization approaches include those by Sigmund and coworkers (Sigmund 1994, 1995, 2000), Gibiansky and Sigmund (2000) and Neves et al. (2000). In these studies, the macroscopic elasticity tensors obtained through computational homogenization are optimized to attain extremal properties, i.e., maximum bulk and shear moduli, negative Poisson's ratio, etc. To carry out topology optimization, the above studies utilize an asymptotic multiscale model for computational homogenization (Bensoussan et al. 1978; Pavliotis and Stuart 2008) along with a design parameterization which can be categorized as density-based (Deaton and Grandhi 2014). Though successful for elastic microstructural design, this paradigm has not been used for the design of inelastic microstructures due to the fact that multiscale models based on asymptotic expansions are difficult to extend to problems with material nonlinearities in a straightforward and general way. Indeed, this has been mentioned as a major impediment to the development of inelastic microstructural design techniques (Osanov and Guest 2016) and has prompted alternative approaches such as the use of finite periodic structures for performing microstructural design (Carstensen et al. 2015). An alternative microstructural design framework is outlined in De Souza Neto et al. (2010) and Amstutz et al. (2010), making use of RVE-based multiscale models for computational homogenization (Hill 1963, 1967; Mandel 1966) and a level set design parameterization which exploits the topological derivative concept (Amstutz and Andra 2006; Giusti et al. 2009). Again, this framework has only been applied to elastic microstructures. In this case, the difficulty in extending the framework comes not from the multiscale modeling approach but from the design parameterization. Hence, to consider topology optimization for the design of inelastic microstructures, both the multiscale modeling approach and the design parameterization must be amenable to the use of inelastic material models.

Unlike the asymptotic approach to multiscale modeling, the RVE-based approach allows for the incorporation of inelastic material models in a straightforward manner. Moreover, this RVE-based approach can be given an axiomatic variational framework (De Souza Neto and Feijoo 2006; Blanco et al. 2016), making it especially suitable for computational homogenization using finite element analysis. Indeed, when performing computational homogenization with nonlinear problems, the most common approach is to employ RVE-based multiscale models with finite element analysis (Geers et al. 2010; Saeb et al. 2016). In this way, macroscale constitutive quantities are numerically obtained as volume averages of the constitutive quantities obtained through the solution of an appropriately defined microscale problem. For these volume averages to provide a meaningful macroscopic response, the microscale problem must be defined over a domain that statistically represents the characteristic microstructural heterogeneities. This domain is known as a representative volume element or RVE. Central to classical homogenization theories is the concept of scale separation, wherein it is assumed that field fluctuations in the material microstructure should be smaller than the size of the RVE and that the RVE should itself be much smaller than the scale of macroscopic field fluctuations (Geers et al. 2010). Based on this, an equilibrium boundary value problem is defined over the RVE domain by applying suitable constraints on boundary terms such that they satisfy a multiscale energetic criterion known as the Hill-Mandel principle (Hill 1963, 1967; Mandel 1966). Following the solution of this boundary value problem, macroscopic constitutive quantities can then be extracted by applying appropriate volume averages. This approach does not restrict the constitutive behavior of the RVE domain and thus provides an avenue for inelastic microstructural design by considering an inelastic RVE domain.

To facilitate the design of an RVE domain requires parameterizing this domain in some way. While both density-based and level-set design parameterizations have been used for elastic microstructural design, the density-based approach is more amenable to the consideration of inelastic material models. This has been demonstrated recently through studies which utilize density-based topology optimization with a number of complicated inelastic models (Zhang et al. 2017; Li et al. 2017a, b; Alberdi and Khandelwal 2017; Alberdi et al. 2018b). On the other hand, the level set approach has been mainly restricted to the realm of linear elastic behavior as the shape derivatives which are needed to drive design updates are difficult to obtain in the case of inelastic materials. Shape derivatives have been derived for an elastoplastic model in Aymeric et al. (2018) using regularization techniques, but this approach cannot be applied generally to different models in the way that a density-based approach can. It should also be mentioned that microstructural topology optimization has been investigated using different parameterization approaches—namely Voigt and Reuss mixing rules and BESO—and that these approaches have been applied to elastoplastic microstructure design in Swan and Arora (1997) and Chen et al. (2018), respectively. However, the generality and flexibility of the density-based approach for handling various material models and finite element formulations while allowing for accurate sensitivity calculations (Alberdi et al. 2018b) makes it attractive for use in developing an inelastic microstructural design paradigm.

In this study, the design of periodic elastoplastic microstructures for maximum energy dissipation is carried out using

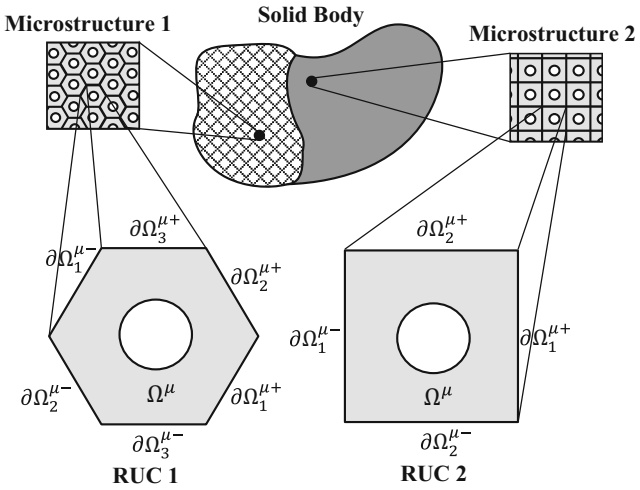

Fig. 1 Solid body with periodic microstructures and corresponding RUCs. Periodic regions of the boundary are shown for each RUC

topology optimization. Computational homogenization is performed using an RVE-based multiscale model and periodicity is enforced through Lagrange multipliers. Hoffman anisotropic plasticity is employed to model the constitutive behavior at the microscale and finite element discretization is done using enhanced assumed strain elements to avoid locking from incompressible plastic flow under plane strain conditions. To parameterize the design problem, a density-based approach is used and material behavior is interpolated with a SIMP-like method (Bendsøe and Sigmund 1999). Accurate sensitivity calculations are achieved by using a path-dependent adjoint method. Attention is devoted to issues such as dependence on initial design and enforcement of microstructural connectivity, and a number of optimized microstructural designs are obtained under different prescribed macroscopic strains. It is also shown that the consideration of plastic anisotropy leads to optimized microstructural topologies which differ from those obtained with the isotropic von Mises model. The remainder of this paper is laid out as follows: Section 2 gives details on the computational homogenization performed with an RVE-based multiscale model and Hoffman anisotropic plasticity, including the discretization using EAS elements and enforcement of periodic boundary constraints with Lagrange multipliers. Section 3 discusses the design parameterization, problem formulation and sensitivity analysis. Section 4 details numerical issues that may arise when designing microstructures and illustrates techniques to handle them. Sections 5 and 6 then present a number of optimized microstructure topologies obtained using anisotropic plasticity. Finally, Section 7 provides the important conclusions.

2 Computational homogenization

For architectured materials with regular periodic microstructures, the microstructural heterogeneities can be identified as belonging to a periodically repeating unit cell. In this case, the representative unit cell (RUC) replaces the RVE as the domain for the microscale problem. As this study focuses on the design of such architectured microstructures, the microscale problem domain will be assumed to be an RUC throughout. That is, the design problem will be defined over an RUC and periodic repetition of the optimized RUC will result in the optimized microstructure. The concept of an RUC is illustrated in Fig. 1 where two different microstructures and their corresponding RUCs are shown.

To perform computational homogenization, relations which prescribe how to obtain the correct volume averages of constitutive quantities are needed in addition to appropriate governing equilibrium equations for the microscale problem, i.e., for the RUC. These homogenization relations and equilibrium equations may be derived in a variety of ways, but for the sake of brevity this section will focus on the description of these equations rather than their derivation. Interested readers are directed to the following references for details on the derivation and theoretical aspects of RVE-based multiscale models (Hill 1963, 1967; Mandel 1966; de Souza Neto and Feijoo 2006; Saeb et al. 2016; Blanco et al. 2016; Alberdi et al. 2018a).

2.1 Kinematics and volume averages

For an RUC domain Ω^μ (Fig. 1), the volume average of a microscopic scalar, vector or tensor field $\boldsymbol{f}$ is obtained as

$$\frac{1}{V}\int_{\Omega^\mu} \boldsymbol{f}\, dv \tag{1}$$

where $V = \int_{\Omega^\mu} dv$ is the total volume of the RUC, including voids. Small deformation theory is considered and the governing kinematical variable in this case is the strain tensor $\boldsymbol{\varepsilon} = \nabla^s \boldsymbol{u}$ where ∇^s is the symmetric gradient operator and $\boldsymbol{u}$ is the displacement field. At the microscale, the displacement field is considered to consist of a homogeneous part driven by the macroscopic strain tensor and a microscale fluctuation field resulting from the heterogeneities, i.e.,

$$\boldsymbol{u}(\boldsymbol{x}) = \bar{\boldsymbol{\varepsilon}}.\boldsymbol{x} + \tilde{\boldsymbol{u}}(\boldsymbol{x}) \quad \forall \quad \boldsymbol{x} \in \Omega^\mu \tag{2}$$

where $\bar{\boldsymbol{\varepsilon}}$ is the macroscopic strain tensor and $\tilde{\boldsymbol{u}}(\boldsymbol{x})$ is the microscale displacement fluctuation field. Here and

for the remainder of the paper quantities with an overbar ($\overline{(\blacksquare)}$) represent macroscopic quantities. The homogenization relation for the strain tensor is given as

$$\overline{\boldsymbol{\varepsilon}} = \frac{1}{V}\int_{\Omega^\mu} \boldsymbol{\varepsilon}(\boldsymbol{x})dv = \frac{1}{V}\int_{\Omega^\mu} (\overline{\boldsymbol{\varepsilon}} + \nabla^s \tilde{\boldsymbol{u}})dv \tag{3}$$

where (2) was used in the second equality. It can be seen that in the absence of microscale fluctuations, this relation is trivially satisfied. Similarly, the homogenization relation for the Cauchy stress tensor is

$$\overline{\boldsymbol{\sigma}} = \frac{1}{V}\int_{\Omega^\mu} \boldsymbol{\sigma}(\boldsymbol{x})dv \tag{4}$$

where $\boldsymbol{\sigma} = \boldsymbol{\Sigma}(\boldsymbol{\varepsilon}) = \boldsymbol{\Sigma}(\overline{\boldsymbol{\varepsilon}} + \nabla^s \tilde{\boldsymbol{u}})$ and the function $\boldsymbol{\Sigma}$ depends on the constitutive model(s) governing the microscopic constituents. It should be noted that there are no requirements that the function $\boldsymbol{\Sigma}$ be elastic, i.e., inelastic constitutive models can be canonically considered within this framework with no loss of generality.

2.2 Hill-Mandel principle

For RVE-based multiscale models, an essential requirement which must be satisfied in the transition between the scales is that the average work done at the microscale should be equivalent to the work done at the macroscale. This energetic relationship is known as the Hill-Mandel principle (Hill 1963, 1967; Mandel 1966) and is stated as

$$\overline{\boldsymbol{\sigma}} : d\overline{\boldsymbol{\varepsilon}} = \frac{1}{V}\int_{\Omega^\mu} \boldsymbol{\sigma} : d\boldsymbol{\varepsilon} dv \tag{5}$$

Hence, to derive meaningful information from an RUC, the stress and strain fields within it must satisfy (5). For periodic metamaterials, this is satisfied if the RUC domain is considered to be in self-equilibrium and the displacement fluctuations on the RUC boundary are periodic. Self-equilibrium of the RUC requires that

$$\nabla.\boldsymbol{\sigma} = \boldsymbol{0} \quad \text{in} \quad \Omega^\mu \tag{6}$$

For displacement fluctuations to be periodic on the RUC boundary $\partial\Omega^\mu$, this boundary is divided into opposing regions $\partial\Omega^{\mu-}$ and $\partial\Omega^{\mu+}$ such that $\partial\Omega^\mu = \partial\Omega^{\mu+} \cup \partial\Omega^{\mu-}$ and $\partial\Omega^{\mu+} \cap \partial\Omega^{\mu-} = \emptyset$. Periodicity requires that the fluctuations $\tilde{\boldsymbol{u}}(\boldsymbol{x}^+) = \tilde{\boldsymbol{u}}(\boldsymbol{x}^-)$ for $\boldsymbol{x}^+ \in \partial\Omega^{\mu+}$ and $\boldsymbol{x}^- \in \partial\Omega^{\mu-}$. Making use of (2), this can be rearranged as

$$\boldsymbol{u}(\boldsymbol{x}^+) - \boldsymbol{u}(\boldsymbol{x}^-) = \overline{\boldsymbol{\varepsilon}}.(\boldsymbol{x}^+ - \boldsymbol{x}^-) \tag{7}$$

Figure 1 shows the periodic boundary regions for both hexagonal and square RUC domains. Here, $\partial\Omega^{\mu+}$ and $\partial\Omega^{\mu-}$ are divided into opposing sides $\partial\Omega_j^{\mu+}$ and $\partial\Omega_j^{\mu-}$ where $j = 3$ for the hexagonal RUC and $j = 2$ for the square RUC. Based on the above requirements, the microscale problem for computational homogenization is given as the following equilibrium boundary value problem on a RUC: find the microscale displacement field $\boldsymbol{u}(\boldsymbol{x})$ such that

$$\begin{aligned} &\nabla.\boldsymbol{\sigma} = \boldsymbol{0} \quad \text{in} \quad \Omega^\mu \\ &\boldsymbol{u}(\boldsymbol{x}^+) - \boldsymbol{u}(\boldsymbol{x}^-) = \overline{\boldsymbol{\varepsilon}}.\boldsymbol{l} \quad \text{on} \quad \partial\Omega^\mu \end{aligned} \tag{8}$$

where $\boldsymbol{l} = \boldsymbol{x}^+ - \boldsymbol{x}^-$ is the distance vector between opposing boundary regions. From (8), it can be seen that the deformation of the RUC is driven by the macroscopic strain tensor $\overline{\boldsymbol{\varepsilon}}$.

Remark: Rather than posing self-equilibrium and restricting boundary terms to satisfy the Hill-Mandel principle as is commonly done (Saeb et al. 2016), the Hill-Mandel principle can be posed as an energetic criterion along with kinematical constraints to derive the self-equilibrium and stress homogenization relations as its consequences (Blanco et al. 2016; Alberdi et al. 2018a). Regardless of the derivation, the resulting RUC equilibrium boundary value problem is the same, i.e. the application of periodic boundary conditions to a given domain governed by linear momentum balance in the absence of body forces and inertia effects (8). This equilibrium boundary value problem may also be derived through other homogenization approaches.

2.3 Hoffmann plasticity

The boundary value problem in (8) is completed with the prescription of the constitutive relations $\boldsymbol{\sigma} = \boldsymbol{\Sigma}(\boldsymbol{\varepsilon})$. In this study, the Hoffman anisotropic plasticity model is considered to describe the constitutive material behavior in an RUC as materials produced by additive manufacturing techniques may show anisotropy in plastic yielding (Frazier 2014; Cantrell et al. 2017). The Hoffman plasticity model is an extension of the Hill orthotropic plasticity model (Hill 1948) to account for different yield stresses under tension and compression (De Souza Neto et al. 2011). Orthotropy is defined by an orthonormal basis $\{\hat{\boldsymbol{e}}_1, \hat{\boldsymbol{e}}_2, \hat{\boldsymbol{e}}_3\}$, which coincides with a set of principal axes of orthotropy. This orthonormal basis can be defined in terms of the global Euclidean basis $\{\boldsymbol{e}_1, \boldsymbol{e}_2, \boldsymbol{e}_3\}$ through the change of basis matrix $[g_{ij}]$ such that $\boldsymbol{e}_i = g_{ij}\hat{\boldsymbol{e}}_j$, $(i, j = 1, 2, 3)$. Along the axes of orthotropy, the Cauchy stress and strain tensor are given in matrix-vector form as

$$\begin{aligned} \hat{\boldsymbol{\sigma}} &= \boldsymbol{T}_1\boldsymbol{\sigma} \\ \hat{\boldsymbol{\varepsilon}} &= \boldsymbol{T}_2\boldsymbol{\varepsilon} \end{aligned} \tag{9}$$

where

$$
\begin{aligned}
\hat{\boldsymbol{\sigma}} &= \left[\begin{array}{cccccc}\hat{\sigma}_{11} & \hat{\sigma}_{22} & \hat{\sigma}_{33} & \hat{\sigma}_{12} & \hat{\sigma}_{23} & \hat{\sigma}_{31}\end{array}\right]^T, \boldsymbol{\sigma} = \left[\begin{array}{cccccc}\sigma_{11} & \sigma_{22} & \sigma_{33} & \sigma_{12} & \sigma_{23} & \sigma_{31}\end{array}\right]^T, \\
\hat{\boldsymbol{\varepsilon}} &= \left[\begin{array}{cccccc}\hat{\varepsilon}_{11} & \hat{\varepsilon}_{22} & \hat{\varepsilon}_{33} & 2\hat{\varepsilon}_{12} & 2\hat{\varepsilon}_{23} & 2\hat{\varepsilon}_{31}\end{array}\right]^T, \boldsymbol{\varepsilon} = \left[\begin{array}{cccccc}\varepsilon_{11} & \varepsilon_{22} & \varepsilon_{33} & 2\varepsilon_{12} & 2\varepsilon_{23} & 2\varepsilon_{31}\end{array}\right]^T, \\
\boldsymbol{T}_1 &= \left[\begin{array}{cccccc}
g_{11}^2 & g_{21}^2 & g_{31}^2 & 2g_{11}g_{21} & 2g_{21}g_{31} & 2g_{11}g_{31} \\
g_{12}^2 & g_{22}^2 & g_{32}^2 & 2g_{12}g_{22} & 2g_{22}g_{32} & 2g_{12}g_{32} \\
g_{13}^2 & g_{23}^2 & g_{33}^2 & 2g_{13}g_{23} & 2g_{23}g_{33} & 2g_{13}g_{33} \\
g_{11}g_{12} & g_{21}g_{22} & g_{31}g_{32} & g_{21}g_{12}+g_{11}g_{22} & g_{31}g_{22}+g_{21}g_{32} & g_{31}g_{12}+g_{11}g_{32} \\
g_{12}g_{13} & g_{22}g_{23} & g_{32}g_{33} & g_{22}g_{13}+g_{12}g_{23} & g_{32}g_{23}+g_{22}g_{33} & g_{32}g_{13}+g_{12}g_{33} \\
g_{13}g_{11} & g_{23}g_{21} & g_{33}g_{31} & g_{23}g_{11}+g_{13}g_{21} & g_{33}g_{21}+g_{23}g_{31} & g_{33}g_{11}+g_{13}g_{31}
\end{array}\right] \\
\boldsymbol{T}_2 &= \left[\begin{array}{cccccc}
g_{11}^2 & g_{21}^2 & g_{31}^2 & g_{11}g_{21} & g_{21}g_{31} & g_{11}g_{31} \\
g_{12}^2 & g_{22}^2 & g_{32}^2 & g_{12}g_{22} & g_{22}g_{32} & g_{12}g_{32} \\
g_{13}^2 & g_{23}^2 & g_{33}^2 & g_{13}g_{23} & g_{23}g_{33} & g_{13}g_{33} \\
2g_{11}g_{12} & 2g_{21}g_{22} & 2g_{31}g_{32} & g_{21}g_{12}+g_{11}g_{22} & g_{31}g_{22}+g_{21}g_{32} & g_{31}g_{12}+g_{11}g_{32} \\
2g_{12}g_{13} & 2g_{22}g_{23} & 2g_{32}g_{33} & g_{22}g_{13}+g_{12}g_{23} & g_{32}g_{23}+g_{22}g_{33} & g_{32}g_{13}+g_{12}g_{33} \\
2g_{13}g_{11} & 2g_{23}g_{21} & 2g_{33}g_{31} & g_{23}g_{11}+g_{13}g_{21} & g_{33}g_{21}+g_{23}g_{31} & g_{33}g_{11}+g_{13}g_{31}
\end{array}\right]
\end{aligned} \tag{10}
$$

Following the standard additive decomposition of the strain tensor, i.e., $\hat{\boldsymbol{\varepsilon}} = \hat{\boldsymbol{\varepsilon}}^e + \hat{\boldsymbol{\varepsilon}}^p$, the Cauchy stress is given by the following elastic constitutive equation along the axes of orthotropy

$$
\hat{\boldsymbol{\sigma}} = \hat{\boldsymbol{C}}^e \hat{\boldsymbol{\varepsilon}}^e \tag{11}
$$

In general, orthotropic plasticity may coincide with an orthotropic elastic tensor $\hat{\boldsymbol{C}}^e$. However, in this study, only isotropic elasticity is considered so that $\hat{\boldsymbol{C}}^e$ is the matrix form of the isotropic elasticity tensor $\mathbb{C}^E = 3\kappa\mathbb{P}_{vol} + 2G\mathbb{P}^s_{dev}$. Here, κ is the bulk modulus, G is the shear modulus and $\mathbb{P}_{vol} \triangleq \frac{1}{3}\boldsymbol{I}\otimes\boldsymbol{I}$ and $\mathbb{P}^s_{dev} \triangleq \mathbb{I}^s_4 - \mathbb{P}_{vol}$ are the fourth order volumetric and symmetric deviatoric projection tensors, respectively, where $[\mathbb{I}^s_4]_{ijkl} = \frac{1}{2}(\delta_{ik}\delta_{jl} + \delta_{il}\delta_{jk})$.

The Hoffman yield function is defined along the axes of orthotropy $\{\hat{\boldsymbol{e}}_1, \hat{\boldsymbol{e}}_2, \hat{\boldsymbol{e}}_3\}$ as

$$
\phi(\hat{\boldsymbol{\sigma}}, \zeta) = \frac{1}{2}\hat{\boldsymbol{\sigma}}^T \boldsymbol{P}\hat{\boldsymbol{\sigma}} + \boldsymbol{q}^T\hat{\boldsymbol{\sigma}} - \zeta^2(\alpha) \tag{12}
$$

where $\zeta(\alpha)$ is a dimensionless relative yield stress which defines the size of the yield surface in the six-dimensional stress-space and $\hat{\boldsymbol{\sigma}}$ is the vector form of the Cauchy stress along the axes of orthotropy $(9)_1$. Linear isotropic strain hardening is adopted in this study so that the dimensionless relative yield stress $\zeta(\alpha)$ is defined in terms of the accumulated plastic strain α and given by

$$
\zeta(\alpha) = 1 + \left(\frac{K^h}{\sigma_y}\right)\alpha \tag{13}
$$

where K^h is the hardening coefficient and σ_y is the initial yield stress. In (12), the matrix $\boldsymbol{P}$ and vector $\boldsymbol{q}$ contain constants pertaining to the yield stresses along different orthotropic axes and are given as

$$
\begin{aligned}
\boldsymbol{P} &= 2\left[\begin{array}{cccccc}
c_1+c_3 & -c_1 & -c_3 & 0 & 0 & 0 \\
-c_1 & c_2+c_1 & -c_2 & 0 & 0 & 0 \\
-c_3 & -c_2 & c_3+c_2 & 0 & 0 & 0 \\
0 & 0 & 0 & c_4 & 0 & 0 \\
0 & 0 & 0 & 0 & c_5 & 0 \\
0 & 0 & 0 & 0 & 0 & c_6
\end{array}\right] \\
\boldsymbol{q} &= \left[\begin{array}{cccccc}c_7 & c_8 & c_9 & 0 & 0 & 0\end{array}\right]^T \\
c_1 &= \frac{1}{2}\left(\frac{1}{\hat{\sigma}^t_{11}\hat{\sigma}^c_{11}} + \frac{1}{\hat{\sigma}^t_{22}\hat{\sigma}^c_{22}} - \frac{1}{\hat{\sigma}^t_{33}\hat{\sigma}^c_{33}}\right) \\
c_2 &= \frac{1}{2}\left(\frac{-1}{\hat{\sigma}^t_{11}\hat{\sigma}^c_{11}} + \frac{1}{\hat{\sigma}^t_{22}\hat{\sigma}^c_{22}} + \frac{1}{\hat{\sigma}^t_{33}\hat{\sigma}^c_{33}}\right) \\
c_3 &= \frac{1}{2}\left(\frac{1}{\hat{\sigma}^t_{11}\hat{\sigma}^c_{11}} - \frac{1}{\hat{\sigma}^t_{22}\hat{\sigma}^c_{22}} + \frac{1}{\hat{\sigma}^t_{33}\hat{\sigma}^c_{33}}\right) \\
c_4 &= \frac{1}{\left(\hat{\sigma}^0_{12}\right)^2},\ c_5 = \frac{1}{\left(\hat{\sigma}^0_{23}\right)^2},\ c_6 = \frac{1}{\left(\hat{\sigma}^0_{13}\right)^2} \\
c_7 &= \frac{\hat{\sigma}^c_{11} - \hat{\sigma}^t_{11}}{\hat{\sigma}^t_{11}\hat{\sigma}^c_{11}},\ c_8 = \frac{\hat{\sigma}^c_{22} - \hat{\sigma}^t_{22}}{\hat{\sigma}^t_{22}\hat{\sigma}^c_{22}},\ c_9 = \frac{\hat{\sigma}^c_{33} - \hat{\sigma}^t_{33}}{\hat{\sigma}^t_{33}\hat{\sigma}^c_{33}}
\end{aligned} \tag{14}
$$

where $\hat{\sigma}^t_{ii}$ and $\hat{\sigma}^c_{ii}$ denote the initial (i.e., when $\alpha = 0$) tensile and compressive direct yield stresses along the axes of orthotropy $\hat{\boldsymbol{e}}_i$ and $\hat{\sigma}^0_{12}$, $\hat{\sigma}^0_{23}$ and $\hat{\sigma}^0_{13}$ denote the initial yield stresses in states of pure shear on the orthotropic planes. If $\hat{\sigma}^c_{11} = \hat{\sigma}^t_{11} = \hat{\sigma}^c_{22} = \hat{\sigma}^t_{22} = \hat{\sigma}^c_{33} = \hat{\sigma}^t_{33} = \sqrt{3}\hat{\sigma}^0_{12} = \sqrt{3}\hat{\sigma}^0_{23} = \sqrt{3}\hat{\sigma}^0_{13}$ the von Mises isotropic yield function is recovered.

An associative flow rule is adopted to describe the evolution of the plastic strain $\hat{\boldsymbol{\varepsilon}}^p$, i.e.

$$\dot{\hat{\boldsymbol{\varepsilon}}}^p = \gamma \frac{\partial \phi}{\partial \hat{\boldsymbol{\sigma}}} = \gamma(\boldsymbol{P}\hat{\boldsymbol{\sigma}} + \boldsymbol{q}) \tag{15}$$

whereas the evolution of the accumulated plastic strain α is given by

$$\dot{\alpha} = \sqrt{\frac{2}{3}\dot{\hat{\boldsymbol{\varepsilon}}}^{pT}\boldsymbol{Z}\dot{\hat{\boldsymbol{\varepsilon}}}^p} \tag{16}$$

$$\begin{aligned} &\phi \leq 0, \quad \gamma \geq 0, \quad \gamma\phi = 0 \\ &\gamma\dot{\phi} = 0 \end{aligned} \tag{17}$$

where $\boldsymbol{Z} = \text{diag}\left[\,1\ 1\ 1\ 0.5\ 0.5\ 0.5\,\right]$. The above flow rules are completed by the KKT and consistency conditions (17), which describe the plastic loading and unloading processes. Details on the numerical implementation of this model using the elastic predictor/plastic return-mapping algorithm are omitted here, as they have been presented elsewhere (De Borst and Feenstra 1990; Schellekens and De Borst 1990; De Souza Neto et al. 2011). The interested readers are directed to Appendix A in Ref. (Zhang et al. (2017)) for details on the implementation of this model in the form presented above.

Remark For all of the examples considered in this study, the material parameters of the Hoffman model are as follows: The initial yield stresses under tension along the axes of orthotropy are set to $\hat{\sigma}^t_{22} = \hat{\sigma}^t_{33} = \sigma_y$ and $\hat{\sigma}^t_{11} = \chi\sigma_y$ where σ_y is the initial yield stress used in the isotropic hardening model (13) and the scalar χ determines the ratio between tensile yield stresses along orthotropic axes $\hat{\boldsymbol{e}}_1$ and $\hat{\boldsymbol{e}}_2$ (or $\hat{\boldsymbol{e}}_3$). The initial yield stresses under compression in each orthotropic direction are set to $\hat{\sigma}^c_{ii} = \omega\hat{\sigma}^t_{ii}$ where ω is another scalar controlling the ratio between compressive and tensile yield stresses. The initial yield stresses in shear along the orthotropic planes are $\hat{\sigma}^0_{ij} = \frac{1}{2\sqrt{3}}\left(\hat{\sigma}^t_{ii} + \hat{\sigma}^t_{jj}\right)$, $i, j = 1, 2, 3$. From these parameters, it can be seen that when $\omega = 1$ and $\chi = 1$ this will result in the von Mises model. Finally, the axes of orthotropy are considered to be rotated in plane from the Cartesian coordinate system, resulting in a change of basis matrix $[g_{ij}]$ which has the form

$$[g_{ij}] = \begin{bmatrix} \cos\theta & -\sin\theta & 0 \\ \sin\theta & \cos\theta & 0 \\ 0 & 0 & 1 \end{bmatrix} \tag{18}$$

where θ is the angle of in-plane rotation.

2.4 Discretization – EAS elements

In this study, computational homogenization is performed using finite element analysis to discretize the RUC equilibrium boundary value problem in (8). To handle the incompressibility associated with plastic flow, this discretization is carried out using enhanced assumed strain (EAS) elements, following the process laid out in Simo and Rifai (1990). Details on the construction of discrete approximations using EAS elements are left out and attention is focused on the resulting discrete form of the RUC equilibrium boundary value problem. After discretization using the appropriate approximating spaces, $(8)_1$ gives

$$\boldsymbol{F}_{int} = \boldsymbol{0} \tag{19}$$

where

$$\begin{aligned} \boldsymbol{F}_{int} &= \mathop{\mathcal{A}}_{e=1}^{n_{ele}} \boldsymbol{F}^e_{int} \\ \boldsymbol{F}^e_{int} &= \boldsymbol{F}^e_{int}(\boldsymbol{u}_e, \tilde{\boldsymbol{\alpha}}_e) = \int_{\Omega^{\mu e}} \boldsymbol{B}^T\boldsymbol{\sigma}\, dv \end{aligned} \tag{20}$$

Here, $\Omega^{\mu e}$ is the domain of element e, $\boldsymbol{u}_e$ is the nodal displacement vector of element e and $\boldsymbol{B}$ is the element shape function derivative matrix. $\mathcal{A}$ denotes the finite element assembly operator, and n_{ele} is the total number of finite elements in the domain. The Hoffman constitutive model at the microscale $\boldsymbol{\sigma} = \boldsymbol{\Sigma}(\boldsymbol{\varepsilon})$ is evaluated in terms of the enhanced strain $\boldsymbol{\varepsilon} \triangleq \boldsymbol{B}\boldsymbol{u}_e + \boldsymbol{G}\tilde{\boldsymbol{\alpha}}_e$ where $\boldsymbol{G}$ is the enhanced strain shape function matrix and $\tilde{\boldsymbol{\alpha}}_e$ is the element level enhanced strain parameter. This study considers plane strain problems where the RUC domain Ω^μ is discretized using four node quadrilateral elements with four enhanced modes (Q1/E4 EAS elements), as proposed in Simo and Rifai (1990).

To enforce the necessary orthogonality between enhanced modes and stresses (Simo and Rifai 1990), additional residual equations are needed at the element level. These equations are

$$\begin{aligned} &\tilde{\boldsymbol{H}}_e(\boldsymbol{u}_e, \tilde{\boldsymbol{\alpha}}_e) = \boldsymbol{0}, \quad e = 1, 2, ...n_{ele} \\ &\tilde{\boldsymbol{H}}_e = \int_{\Omega^{\mu e}} \boldsymbol{G}^T\boldsymbol{\sigma}\, dv \end{aligned} \tag{21}$$

To eliminate the degrees of freedom $\tilde{\boldsymbol{\alpha}}_e$ from the global system of equations, $(21)_2$ is solved for each element to obtain $\tilde{\boldsymbol{\alpha}}_e$ using the Newton-Raphson method (Kasper and Taylor 1997, 2000). This necessitates the use of the element level tangent matrix, given as

$$\boldsymbol{K}^e_{\tilde{\alpha}\tilde{\alpha}} = \frac{d\tilde{\boldsymbol{H}}}{d\tilde{\boldsymbol{\alpha}}_e} = \int_{\Omega^{\mu e}} \boldsymbol{G}^T[\mathbb{C}_T]\boldsymbol{G}\, dv \tag{22}$$

where $\mathbb{C}_T$ is is the algorithmic consistent tangent modulus coming from the constitutive model. After the degrees of freedom $\tilde{\boldsymbol{\alpha}}_e$ are solved for at the element level, the global residual (19) is defined only in terms of the displacement degrees of freedom.

The RUC boundary value problem also requires enforcing the periodic constraints $(8)_2$. These are enforced pointwise so that they are directly applied to degrees of freedom

on the discretized RUC boundary. The discrete form of $(8)_2$ yields the following constraints

$$\boldsymbol{A}\boldsymbol{u} - \boldsymbol{L}\hat{\bar{\boldsymbol{\varepsilon}}} = \boldsymbol{0} \tag{23}$$

where $\boldsymbol{u}$ is the vector of global displacement degrees of freedom and in two dimensions $\hat{\bar{\boldsymbol{\varepsilon}}} = \left[\, \bar{\varepsilon}_{11} \;\; \bar{\varepsilon}_{22} \;\; 2\bar{\varepsilon}_{12} \,\right]^T$. The constraint matrix $\boldsymbol{A}$ relates degrees of freedom on opposing regions of the RUC boundary while the matrix $\boldsymbol{L}$ contains the distances $l_1 = x^+ - x^-$ and $l_2 = y^+ - y^-$ between these opposing sides. For the i^{th} pair of boundary nodes, these matrices have the form

$$\boldsymbol{A}^i\boldsymbol{u}^i - \boldsymbol{L}^i\hat{\bar{\boldsymbol{\varepsilon}}} = \begin{bmatrix} 1 & 0 & -1 & 0 \\ 0 & 1 & 0 & -1 \end{bmatrix} \begin{bmatrix} u_i^+ \\ v_i^+ \\ u_i^- \\ v_i^- \end{bmatrix} - \begin{bmatrix} l_1 & 0 & l_2/2 \\ 0 & l_2 & l_1/2 \end{bmatrix} \begin{bmatrix} \bar{\varepsilon}_{11} \\ \bar{\varepsilon}_{22} \\ 2\bar{\varepsilon}_{12} \end{bmatrix} = \begin{bmatrix} 0 \\ 0 \end{bmatrix} \tag{24}$$

The discrete constraint (23) can be enforced in different ways including direct elimination (Saeb et al. 2016) and Lagrange multiplier (Miehe and Koch 2002) approaches. The Lagrange multiplier approach is adopted in this study, so that the global system of equations which must be solved for RUC equilibrium is

$$\boldsymbol{R}(\boldsymbol{u}, \boldsymbol{\gamma}) = \begin{bmatrix} \boldsymbol{R}_1(\boldsymbol{u}, \boldsymbol{\gamma}) \\ \boldsymbol{R}_2(\boldsymbol{u}) \end{bmatrix} = \begin{bmatrix} \boldsymbol{F}_{int}(\boldsymbol{u}) + \boldsymbol{A}^T\boldsymbol{\gamma} \\ \boldsymbol{A}\boldsymbol{u} - \boldsymbol{L}\hat{\bar{\boldsymbol{\varepsilon}}} \end{bmatrix} = \begin{bmatrix} \boldsymbol{0} \\ \boldsymbol{0} \end{bmatrix} \tag{25}$$

where $\boldsymbol{\gamma}$ is a vector of Lagrange multipliers that enforce periodic boundary constraints. As the constitutive models used in this study consider nonlinear inelastic behavior, (25) is a nonlinear algebraic system that is solved using the Newton-Raphson method, requiring the Jacobian matrix

$$\boldsymbol{J} = \begin{bmatrix} \dfrac{\partial \boldsymbol{R}_1}{\partial \boldsymbol{u}} & \dfrac{\partial \boldsymbol{R}_1}{\partial \boldsymbol{\gamma}} \\ \dfrac{\partial \boldsymbol{R}_2}{\partial \boldsymbol{u}} & \dfrac{\partial \boldsymbol{R}_2}{\partial \boldsymbol{\gamma}} \end{bmatrix} = \begin{bmatrix} \boldsymbol{K}_T & \boldsymbol{A}^T \\ \boldsymbol{A} & \boldsymbol{0} \end{bmatrix} \tag{26}$$

where $\boldsymbol{K}_T$ is the global tangent stiffness matrix, defined as

$$\boldsymbol{K}_T = \mathop{\mathcal{A}}_{e=1}^{n_{ele}} \boldsymbol{K}_T^e$$
$$\boldsymbol{K}_T^e = \int_{\Omega^{\mu e}} \boldsymbol{B}^T \mathbb{C}_T \boldsymbol{B} dv \tag{27}$$

2.5 Macroscopic stress and tangent moduli

Using the above-described Lagrange multiplier enforcement of the periodic constraints allows for the homogenized Cauchy stress (4) to be obtained equivalently in terms of the Lagrange multipliers $\boldsymbol{\gamma}$ (Miehe and Koch 2002), i.e.,

$$\hat{\bar{\boldsymbol{\sigma}}} = -\frac{1}{V}\boldsymbol{L}^T\boldsymbol{\gamma} \tag{28}$$

where $\hat{\bar{\boldsymbol{\sigma}}} = \left[\, \bar{\sigma}_{11} \;\; \bar{\sigma}_{22} \;\; \bar{\sigma}_{12} \,\right]^T$. Additionally, the homogenized tangent moduli tensor $\bar{\mathbb{C}}$, which relates increments of the homogenized Cauchy stress $\bar{\boldsymbol{\sigma}}$ to increments of the homogenized strain tensor $\bar{\boldsymbol{\varepsilon}}$, i.e. $d\bar{\boldsymbol{\sigma}} = \bar{\mathbb{C}} : d\bar{\boldsymbol{\varepsilon}}$, can be obtained by linearizing (28), giving

$$d\hat{\bar{\boldsymbol{\sigma}}} = -\frac{1}{V}\boldsymbol{L}^T \frac{\partial \boldsymbol{\gamma}}{\partial \hat{\bar{\boldsymbol{\varepsilon}}}} d\hat{\bar{\boldsymbol{\varepsilon}}} \tag{29}$$

The derivative $\partial\boldsymbol{\gamma}/\partial\hat{\bar{\boldsymbol{\varepsilon}}}$ is calculated by linearizing (25) as

$$\begin{bmatrix} d\boldsymbol{R}_1 \\ d\boldsymbol{R}_2 \end{bmatrix} = \begin{bmatrix} \dfrac{\partial \boldsymbol{R}_1}{\partial \boldsymbol{u}} & \dfrac{\partial \boldsymbol{R}_1}{\partial \boldsymbol{\gamma}} \\ \dfrac{\partial \boldsymbol{R}_2}{\partial \boldsymbol{u}} & \dfrac{\partial \boldsymbol{R}_2}{\partial \boldsymbol{\gamma}} \end{bmatrix} \begin{bmatrix} d\boldsymbol{u} \\ d\boldsymbol{\gamma} \end{bmatrix} + \begin{bmatrix} \dfrac{\partial \boldsymbol{R}_1}{\partial \hat{\bar{\boldsymbol{\varepsilon}}}} \\ \dfrac{\partial \boldsymbol{R}_2}{\partial \hat{\bar{\boldsymbol{\varepsilon}}}} \end{bmatrix} d\hat{\bar{\boldsymbol{\varepsilon}}} = \begin{bmatrix} \boldsymbol{0} \\ \boldsymbol{0} \end{bmatrix} \quad \text{or}$$
$$\begin{bmatrix} \boldsymbol{K}_T & \boldsymbol{A}^T \\ \boldsymbol{A} & \boldsymbol{0} \end{bmatrix} \begin{bmatrix} d\boldsymbol{u} \\ d\boldsymbol{\gamma} \end{bmatrix} + \begin{bmatrix} \boldsymbol{0} \\ -\boldsymbol{L} \end{bmatrix} d\hat{\bar{\boldsymbol{\varepsilon}}} = \begin{bmatrix} \boldsymbol{0} \\ \boldsymbol{0} \end{bmatrix} \tag{30}$$

Writing (30) compactly gives

$$d\boldsymbol{R} = \boldsymbol{J}d\hat{\boldsymbol{u}} - \boldsymbol{D}d\hat{\bar{\boldsymbol{\varepsilon}}} = \boldsymbol{0} \tag{31}$$

where $\hat{\boldsymbol{u}} = \left[\, \boldsymbol{u};\; \boldsymbol{\gamma} \,\right]^T$ and $\boldsymbol{D} = \left[\, \boldsymbol{0};\; -\boldsymbol{L} \,\right]^T$, and it can be seen that

$$d\hat{\boldsymbol{u}} = \boldsymbol{S}d\hat{\bar{\boldsymbol{\varepsilon}}} \tag{32}$$

where $\boldsymbol{S} = \boldsymbol{J}^{-1}\boldsymbol{D}$, which is computed by solving the corresponding linear system. Moreover, linearizing (28) yields

$$d\hat{\bar{\boldsymbol{\sigma}}} = -\frac{1}{V}\boldsymbol{D}^T d\hat{\boldsymbol{u}} = -\frac{1}{V}\boldsymbol{D}^T\boldsymbol{S}d\hat{\bar{\boldsymbol{\varepsilon}}} \tag{33}$$

where (32) was used. Equation (33) thus shows that the incremental homogenized tangent moduli tensor is

$$\bar{\mathbb{C}} = -\frac{1}{V}\boldsymbol{D}^T\boldsymbol{S} \tag{34}$$

Note that for the considered Hoffmann plasticity model in the RUC the incremental homogenized tangent moduli tensor $\bar{\mathbb{C}}$ evolves with the evolution of plasticity.

3 Design parameterization and sensitivity analysis

In this study, a density-based design parameterization is used to perform topology optimization. The details of this parameterization are given in this section along with the optimization problem formulation and sensitivity information needed for use with the gradient based optimizer.

3.1 Density-based design parameterization

A density-based parameterization assigns each element in a discretized domain a density variable ρ_e which represents

whether the element is empty ($\rho_e = 0$) or contains material ($\rho_e = 1$). This density variable is then relaxed to be continuous, i.e. $0 \leq \rho_e \leq 1$, so that a computationally intensive integer programming problem is transformed to a more amenable nonlinear programming problem. However, with this approach the success of the optimizer depends on the interpolation scheme used to parameterize the material behavior in terms of the element density variable ρ_e. These material interpolation schemes are used to steer designs to different local minima in the case of non-convex optimization problems and also to ensure that density variables in the final design have values of 0 or 1 and thus represent physically meaningful material (or void). In this study, a SIMP-like interpolation scheme (Bendsøe and Sigmund 1999) is utilized, which for a given material parameter A is

$$A_e = [\epsilon_0 + (1 - \epsilon_0)\rho_e^{p_0}]A_0 \tag{35}$$

where A_0 is the parameter value for bulk material, ϵ_0 is a lower bound to characterize void elements and p_0 is a penalization parameter. For the Hoffman plasticity model utilized herein, interpolation of the elastic parameters (i.e., Young's modulus E) is done with (35), while interpolation of the plastic material parameters ($\hat{\sigma}_{ii}^c, \hat{\sigma}_{ii}^t, \hat{\sigma}_{ij}^0$) is done using

$$B_e = [\epsilon_1 + (1 - \epsilon_1)\rho_e^{p_1}]B_0 \tag{36}$$

where B_0 is the plastic parameter value in bulk material and ϵ_1 and p_1 are again a lower bound and penalization parameter, respectively. Choosing $\epsilon_0 \neq \epsilon_1$ and $p_0 \neq p_1$ allows for numerical convergence issues caused by large plastic strains occurring in low density and void elements to be avoided (Maute et al. 1998; Kato et al. 2015; Zhang et al. 2017). The lower bound values used in this study are $\epsilon_0 = 10^{-8}$ and $\epsilon_1 = 10^{-4}$, while the penalization parameters p_0 and p_1 will be discussed in Section 4. The density variables ρ_e used for the above material interpolation are obtained as a weighted average of the design variables of neighboring elements following a standard density filtering procedure which accounts for the periodicity of the RUC domain. In this way, mesh-independency is ensured and topological length scale can be controlled.

3.2 Maximum plastic work problem formulation

The intent of this study is to design elastoplastic microstructures which can dissipate the maximum amount of energy with a prescribed amount of material under a deformation mode specified by the macroscopic strain tensor $\overline{\boldsymbol{\varepsilon}}$. For this purpose, the total plastic work in a RUC is utilized. The total plastic work in the RUC over the entire history of loading is given as

$$W^p = \int_t \int_{\Omega^\mu} \boldsymbol{\sigma} : \dot{\boldsymbol{\varepsilon}}^p d\nu dt \tag{37}$$

The optimization problem is then formulated to maximize the plastic work subjected to a material volume fraction constraint and results in the following constrained optimization problem

$$\begin{aligned}
\min_{\boldsymbol{x}} \quad & f_0(\boldsymbol{x}) = -W^p \\
\text{s.t.} \quad & f_1(\boldsymbol{x}) = \frac{1}{V}\sum_{e=1}^{n_{ele}} \rho_e(\boldsymbol{x}) v_e - V_f \leq 0 \\
& \boldsymbol{R}^k(\hat{\boldsymbol{u}}^k, \hat{\boldsymbol{u}}^{k-1}, \boldsymbol{c}^k, \boldsymbol{c}^{k-1}, \boldsymbol{\rho}(\boldsymbol{x})) = \boldsymbol{0}, \quad k = 1, 2, ..., n \\
& \boldsymbol{H}^k(\hat{\boldsymbol{u}}^k, \hat{\boldsymbol{u}}^{k-1}, \boldsymbol{c}^k, \boldsymbol{c}^{k-1}, \boldsymbol{\rho}(\boldsymbol{x})) = \boldsymbol{0}, \quad k = 1, 2, ..., n \\
& \boldsymbol{0} \leq \boldsymbol{x} \leq \boldsymbol{1}
\end{aligned} \tag{38}$$

where V is the total volume of the RUC design domain, v_e is the volume of element e and V_f is the prescribed volume fraction. The vector $\boldsymbol{x}$ contains design variables which are linearly mapped by the density filter to the vector $\boldsymbol{\rho}$ of density variables.

The system represented in (38) is a PDE-constrained optimization problem wherein constraint $\boldsymbol{R}^k = \boldsymbol{0}$ represents the global RUC equilibrium equations and $\boldsymbol{H}^k = \boldsymbol{0}$ represents the local element EAS elimination and integration point constitutive equations. These constraints are enforced implicitly through FEA in a nested approach where the design variables $\boldsymbol{x}$ are updated by the optimizer and then used in FEA. Once FEA has terminated, the objective and constraint functions are evaluated. During FEA, the initial value problems describing the evolution of internal variables which characterize material history dependence are evaluated by discretizing the deformation history into n pseudo-time steps. Thus, the implicit constraints $\boldsymbol{R}^k = \boldsymbol{0}$ and $\boldsymbol{H}^k = \boldsymbol{0}$ are enforced at each pseudo-time step k. At step k, internal variables are updated using previous step and current step information and so the implicit constraints are functionally dependent on this data, represented by a set of global variables $\hat{\boldsymbol{u}}$ and local variables $\boldsymbol{c}$. Furthermore, these constraints are dependent on the density variables $\boldsymbol{\rho}$ through material interpolation (35 and 36). Hence, they have the functional form shown in (38). While there is no unique way to formulate the constraint sets $\boldsymbol{R}^k$ and $\boldsymbol{H}^k$, there is a minimum number of independent variables $\hat{\boldsymbol{u}}$ and $\boldsymbol{c}$ which are necessary for evaluating the objective and constraint functions. Beyond this minimum set, additional variables may be considered so long as the appropriate constraints are included in $\boldsymbol{R}^k$ and $\boldsymbol{H}^k$. Additional variables may be considered, for example, to simplify complex chain

rule expansions of certain derivatives needed for sensitivity analysis (Alberdi et al. 2018b).

3.3 Path-dependent adjoint sensitivity

The sensitivity calculations needed for gradient based optimization are carried out using the adjoint method as the number of design variables far exceeds the number of response functions considered (Strang 2007; Alberdi et al. 2018b). For sensitivity information to be accurate, the implicit constraints $\boldsymbol{R}^k = \boldsymbol{0}$ and $\boldsymbol{H}^k = \boldsymbol{0}$ at every pseudo-time step during FEA must be considered. Thus, the sensitivity analysis inherits the path-dependence of the material response through these constraints. If a response function f — which can represent an objective or constraint function — is evaluated using the state of a path-dependent material, it depends on the entire deformation history and so has the functional form

$$f(\boldsymbol{x}) = F(\hat{\boldsymbol{u}}^1, ..., \hat{\boldsymbol{u}}^n, \boldsymbol{c}^1, ..., \boldsymbol{c}^n, \boldsymbol{\rho}(\boldsymbol{x})) \tag{39}$$

For sensitivity analysis, the derivative with respect to the design variables $\boldsymbol{x}$ is sought and the application of the density filter is accounted for by applying the chain rule. Thus, the derivative $df/d\boldsymbol{\rho}$ must be calculated. To calculate this using the adjoint method, an augmented function $\hat{f}$ is first constructed as

$$\hat{f} = f(\boldsymbol{\rho}) + \sum_{k=1}^{n} \boldsymbol{\lambda}^{k^T} \boldsymbol{R}^k + \sum_{k=1}^{n} \boldsymbol{\mu}^{k^T} \boldsymbol{H}^k \tag{40}$$

where $\boldsymbol{\lambda}^k$ and $\boldsymbol{\mu}^k$ are the adjoint variables associated with constraints $\boldsymbol{R}^k$ and $\boldsymbol{H}^k$, respectively. As these constraints are enforced to be 0, $d\hat{f}/d\boldsymbol{\rho}$ is equivalent to $df/d\boldsymbol{\rho}$. Expanding $d\hat{f}/d\boldsymbol{\rho}$ using the chain rule gives

$$\begin{aligned}
\frac{df}{d\boldsymbol{\rho}} = \frac{d\hat{f}}{d\boldsymbol{\rho}} &= \frac{\partial F}{\partial \boldsymbol{\rho}} + \sum_{k=1}^{n} \left(\frac{\partial F}{\partial \hat{\boldsymbol{u}}^k} \frac{d\hat{\boldsymbol{u}}^k}{d\boldsymbol{\rho}} + \frac{\partial F}{\partial \boldsymbol{c}^k} \frac{d\boldsymbol{c}^k}{d\boldsymbol{\rho}} \right) \\
&+ \sum_{k=1}^{n} \boldsymbol{\lambda}^{k^T} \left(\frac{\partial \boldsymbol{R}^k}{\partial \boldsymbol{\rho}} + \frac{\partial \boldsymbol{R}^k}{\partial \hat{\boldsymbol{u}}^k} \frac{d\hat{\boldsymbol{u}}^k}{d\boldsymbol{\rho}} + \frac{\partial \boldsymbol{R}^k}{\partial \hat{\boldsymbol{u}}^{k-1}} \frac{d\hat{\boldsymbol{u}}^{k-1}}{d\boldsymbol{\rho}} \right. \\
&\left. + \frac{\partial \boldsymbol{R}^k}{\partial \boldsymbol{c}^k} \frac{d\boldsymbol{c}^k}{d\boldsymbol{\rho}} + \frac{\partial \boldsymbol{R}^k}{\partial \boldsymbol{c}^{k-1}} \frac{d\boldsymbol{c}^{k-1}}{d\boldsymbol{\rho}} \right) \\
&+ \sum_{k=1}^{n} \boldsymbol{\mu}^{k^T} \left(\frac{\partial \boldsymbol{H}^k}{\partial \boldsymbol{\rho}} + \frac{\partial \boldsymbol{H}^k}{\partial \hat{\boldsymbol{u}}^k} \frac{d\hat{\boldsymbol{u}}^k}{d\boldsymbol{\rho}} + \frac{\partial \boldsymbol{H}^k}{\partial \hat{\boldsymbol{u}}^{k-1}} \frac{d\hat{\boldsymbol{u}}^{k-1}}{d\boldsymbol{\rho}} \right. \\
&\left. + \frac{\partial \boldsymbol{H}^k}{\partial \boldsymbol{c}^k} \frac{d\boldsymbol{c}^k}{d\boldsymbol{\rho}} + \frac{\partial \boldsymbol{H}^k}{\partial \boldsymbol{c}^{k-1}} \frac{d\boldsymbol{c}^{k-1}}{d\boldsymbol{\rho}} \right)
\end{aligned} \tag{41}$$

By manipulating the above equation, the implicit derivatives $d\hat{\boldsymbol{u}}^k/d\boldsymbol{\rho}$ and $d\boldsymbol{c}^k/d\boldsymbol{\rho}$ can be eliminated by choosing adjoint variables which satisfy the following adjoint system

$$n^{th}\ step: \begin{cases} \dfrac{\partial F}{\partial \hat{\boldsymbol{u}}^n} + \boldsymbol{\lambda}^{n^T} \dfrac{\partial \boldsymbol{R}^n}{\partial \hat{\boldsymbol{u}}^n} + \boldsymbol{\mu}^{n^T} \dfrac{\partial \boldsymbol{H}^n}{\partial \hat{\boldsymbol{u}}^n} = \boldsymbol{0} \\ \dfrac{\partial F}{\partial \boldsymbol{c}^n} + \boldsymbol{\lambda}^{n^T} \dfrac{\partial \boldsymbol{R}^n}{\partial \boldsymbol{c}^n} + \boldsymbol{\mu}^{n^T} \dfrac{\partial \boldsymbol{H}^n}{\partial \boldsymbol{c}^n} = \boldsymbol{0} \end{cases}$$

$$k^{th}\ step: \begin{cases} \dfrac{\partial F}{\partial \hat{\boldsymbol{u}}^k} + \boldsymbol{\lambda}^{k+1^T} \dfrac{\partial \boldsymbol{R}^{k+1}}{\partial \hat{\boldsymbol{u}}^k} + \boldsymbol{\mu}^{k+1^T} \dfrac{\partial \boldsymbol{H}^{k+1}}{\partial \hat{\boldsymbol{u}}^k} \\ \qquad + \boldsymbol{\lambda}^{k^T} \dfrac{\partial \boldsymbol{R}^k}{\partial \hat{\boldsymbol{u}}^k} + \boldsymbol{\mu}^{k^T} \dfrac{\partial \boldsymbol{H}^k}{\partial \hat{\boldsymbol{u}}^k} = \boldsymbol{0} \\ \dfrac{\partial F}{\partial \boldsymbol{c}^k} + \boldsymbol{\lambda}^{k+1^T} \dfrac{\partial \boldsymbol{R}^{k+1}}{\partial \boldsymbol{c}^k} + \boldsymbol{\mu}^{k+1^T} \dfrac{\partial \boldsymbol{H}^{k+1}}{\partial \boldsymbol{c}^k} \\ \qquad + \boldsymbol{\lambda}^{k^T} \dfrac{\partial \boldsymbol{R}^k}{\partial \boldsymbol{c}^k} + \boldsymbol{\mu}^{k^T} \dfrac{\partial \boldsymbol{H}^k}{\partial \boldsymbol{c}^k} = \boldsymbol{0} \end{cases}$$

$$k = n-1, ..., 2, 1 \tag{42}$$

This system is solved by starting at step n and ending at step 1 and after its solution, (41) is simplified as

$$\frac{df}{d\boldsymbol{\rho}} = \frac{d\hat{f}}{d\boldsymbol{\rho}} = \frac{\partial F}{\partial \boldsymbol{\rho}} + \sum_{k=1}^{n} \left(\boldsymbol{\lambda}^{k^T} \frac{\partial \boldsymbol{R}^k}{\partial \boldsymbol{\rho}} + \boldsymbol{\mu}^{k^T} \frac{\partial \boldsymbol{H}^k}{\partial \boldsymbol{\rho}} \right) \tag{43}$$

Thus, the following derivatives are needed to evaluate (42) and (43):

$$\text{For } \boldsymbol{R}^k: \begin{cases} \frac{\partial \boldsymbol{R}^k}{\partial \boldsymbol{\rho}} \\ \frac{\partial \boldsymbol{R}^k}{\partial \hat{\boldsymbol{u}}^k} \\ \frac{\partial \boldsymbol{R}^k}{\partial \hat{\boldsymbol{u}}^{k-1}} \\ \frac{\partial \boldsymbol{R}^k}{\partial \boldsymbol{c}^k} \\ \frac{\partial \boldsymbol{R}^k}{\partial \boldsymbol{c}^{k-1}} \end{cases} \text{For } \boldsymbol{H}^k: \begin{cases} \frac{\partial \boldsymbol{H}^k}{\partial \boldsymbol{\rho}} \\ \frac{\partial \boldsymbol{H}^k}{\partial \hat{\boldsymbol{u}}^k} \\ \frac{\partial \boldsymbol{H}^k}{\partial \hat{\boldsymbol{u}}^{k-1}} \\ \frac{\partial \boldsymbol{H}^k}{\partial \boldsymbol{c}^k} \\ \frac{\partial \boldsymbol{H}^k}{\partial \boldsymbol{c}^{k-1}} \end{cases} \text{For } F: \begin{cases} \frac{\partial F}{\partial \boldsymbol{\rho}} \\ \frac{\partial F}{\partial \hat{\boldsymbol{u}}^k} \\ \frac{\partial F}{\partial \boldsymbol{c}^k} \end{cases} \tag{44}$$

For the Hoffman plasticity model using EAS elements, the set of local variables $\boldsymbol{c}^k$ is taken as

$$\boldsymbol{c}^k = \left[\boldsymbol{c}_1^k \ ... \ \boldsymbol{c}_{n_{ele}}^k \right]^T \text{ with } \boldsymbol{c}_e^k = \left[\boldsymbol{c}_{e_1}^k \ \boldsymbol{c}_{e_2}^k \ \boldsymbol{c}_{e_3}^k \ \boldsymbol{c}_{e_4}^k \ \tilde{\boldsymbol{\alpha}}_e^k \right]^T \tag{45}$$

where $\boldsymbol{c}_{e_r}^k = \left[\boldsymbol{\sigma}_{e_r}^k \ \boldsymbol{\varepsilon}_{e_r}^{p^k} \ \alpha_{e_r}^k \ \Delta\gamma_{e_r}^k \right]$ is the set of internal variables chosen to represent the coupled constitutive equations. It should be noted that this set is larger than the minimum necessary set, but is chosen because including extra terms reduces some chain rule expansions in the derivatives needed for sensitivity. For this choice of $\boldsymbol{c}^k$, the corresponding local constraint set $\boldsymbol{H}^k$ and its derivatives are discussed in Ref. Zhang et al. (2017) and so are not elaborated upon here, but are provided in Appendix A for completeness.

The set of global variables $\hat{\boldsymbol{u}}^k$ and corresponding global constraints $\boldsymbol{R}^k$ are chosen based on the system in (25) representing RUC equilibrium. That is,

$$\hat{\boldsymbol{u}}^k = \begin{bmatrix} \boldsymbol{u}^k \\ \boldsymbol{\gamma}^k \end{bmatrix}; \quad \boldsymbol{R}^k = \begin{bmatrix} \boldsymbol{R}_1^k \\ \boldsymbol{R}_2^k \end{bmatrix} = \begin{bmatrix} \overset{n_{ele}}{\underset{e=1}{\mathcal{A}}} \boldsymbol{F}_{int}^{e^k} + \boldsymbol{A}^T \boldsymbol{\gamma}^k \\ \boldsymbol{A}\boldsymbol{u}^k - \boldsymbol{L}\hat{\bar{\boldsymbol{\varepsilon}}} \end{bmatrix} \tag{46}$$

where $\boldsymbol{F}_{int}^{e^k} = \sum_{r=1}^{n_{ipt}} \boldsymbol{B}_r^T \boldsymbol{\sigma}_{e_r}^k w_r$ and w_r is the weight of the r^{th} integration point. The derivatives of $\boldsymbol{R}^k$ with respect to the global variables $\hat{\boldsymbol{u}}$ are

$$\frac{\partial \boldsymbol{R}^k}{\partial \hat{\boldsymbol{u}}^{k-1}} = \boldsymbol{0}; \quad \frac{\partial \boldsymbol{R}^k}{\partial \hat{\boldsymbol{u}}^k} = \begin{bmatrix} \boldsymbol{0} & \boldsymbol{A}^T \\ \boldsymbol{A} & \boldsymbol{0} \end{bmatrix} \tag{47}$$

while the derivative $\partial \boldsymbol{R}^k / \partial \boldsymbol{\rho} = \boldsymbol{0}$. The derivatives of $\boldsymbol{R}^k$ with respect to $\boldsymbol{c}$ are

$$\frac{\partial \boldsymbol{R}^k}{\partial \boldsymbol{c}^{k-1}} = \boldsymbol{0}; \quad \frac{\partial \boldsymbol{R}^k}{\partial \boldsymbol{c}^k} = \begin{bmatrix} \overset{n_{ele}}{\underset{e=1}{\mathcal{A}}} \left(\dfrac{\partial \boldsymbol{F}_{int}^{e^k}}{\partial \boldsymbol{c}^k} \right) \\ \boldsymbol{0} \end{bmatrix};$$

$$\frac{\partial \boldsymbol{F}_{int}^{e^k}}{\partial \boldsymbol{c}^k} = \begin{bmatrix} \dfrac{\partial \boldsymbol{F}_{int}^{e^k}}{\partial \boldsymbol{c}_1^k} & \cdots & \dfrac{\partial \boldsymbol{F}_{int}^{e^k}}{\partial \boldsymbol{c}_{n_{ele}}^k} \end{bmatrix} \tag{48}$$

The term $\partial \boldsymbol{F}_{int}^{e^k} / \partial \boldsymbol{c}_j^k$ is nonzero only when $e = j$ and is given as

$$\frac{\partial \boldsymbol{F}_{int}^{e^k}}{\partial \boldsymbol{c}_e^k} = \begin{bmatrix} \dfrac{\partial \boldsymbol{F}_{int}^{e^k}}{\partial \boldsymbol{c}_{e_1}^k} & \dfrac{\partial \boldsymbol{F}_{int}^{e^k}}{\partial \boldsymbol{c}_{e_2}^k} & \dfrac{\partial \boldsymbol{F}_{int}^{e^k}}{\partial \boldsymbol{c}_{e_3}^k} & \dfrac{\partial \boldsymbol{F}_{int}^{e^k}}{\partial \boldsymbol{c}_{e_4}^k} & \dfrac{\partial \boldsymbol{F}_{int}^{e^k}}{\partial \tilde{\boldsymbol{\alpha}}_e^k} \end{bmatrix}$$

$$\frac{\partial \boldsymbol{F}_{int}^{e^k}}{\partial \boldsymbol{c}_{e_r}^k} = \begin{bmatrix} w_r \boldsymbol{B}_r^T & \boldsymbol{0} & \boldsymbol{0} & \boldsymbol{0} \end{bmatrix}; \quad \frac{\partial \boldsymbol{F}_{int}^{e^k}}{\partial \tilde{\boldsymbol{\alpha}}_e^k} = \boldsymbol{0} \tag{49}$$

As the derivative of the volume fraction constraint f_1 in (38) is trivial, it is omitted here. The remaining response function is the objective function f_0. Thus, the derivatives of F which are needed in this study require derivatives of the total plastic work W^p. The trapezoid rule is used to evaluate W^p, giving

$$W^p = \sum_{e=1}^{n_{ele}} \left(\sum_{r=1}^{n_{ipt}} \left(\sum_{k=1}^{n} \left(\frac{1}{2} w_r \left(\boldsymbol{\sigma}_{e_r}^k + \boldsymbol{\sigma}_{e_r}^{k-1} \right) : \left(\boldsymbol{\varepsilon}_{e_r}^{p^k} - \boldsymbol{\varepsilon}_{e_r}^{p^{k-1}} \right) \right) \right) \right) \tag{50}$$

and from this it can be seen that the only nonzero derivative is

$$\frac{\partial W^p}{\partial \boldsymbol{c}^k} = \begin{bmatrix} \dfrac{\partial W^p}{\partial \boldsymbol{c}_1^k} & \dfrac{\partial W^p}{\partial \boldsymbol{c}_2^k} & \cdots & \dfrac{\partial W^p}{\partial \boldsymbol{c}_{n_{ele}}^k} \end{bmatrix} \quad \text{with}$$

$$\frac{\partial W^p}{\partial \boldsymbol{c}_e^k} = \begin{bmatrix} \dfrac{\partial W^p}{\partial \boldsymbol{c}_{e_1}^k} & \dfrac{\partial W^p}{\partial \boldsymbol{c}_{e_2}^k} & \dfrac{\partial W^p}{\partial \boldsymbol{c}_{e_3}^k} & \dfrac{\partial W^p}{\partial \boldsymbol{c}_{e_4}^k} & \dfrac{\partial W^p}{\partial \tilde{\boldsymbol{\alpha}}_e^k} \end{bmatrix} \tag{51}$$

where $\partial W^p / \partial \tilde{\boldsymbol{\alpha}}_e^k = \boldsymbol{0}$ and $\partial W^p / \partial \boldsymbol{c}_{e_r}^k$ is

$$\begin{aligned} &\text{for} \quad k = n \\ &\frac{\partial W^p}{\partial \boldsymbol{c}_{e_r}^n} = \begin{bmatrix} \frac{1}{2} \left(\boldsymbol{\varepsilon}_{e_r}^{p^n} - \boldsymbol{\varepsilon}_{e_r}^{p^{n-1}} \right) w_r & \frac{1}{2} \left(\boldsymbol{\sigma}_{e_r}^n + \boldsymbol{\sigma}_{e_r}^{n-1} \right) w_r & 0 & 0 \end{bmatrix} \\ &\text{for} \quad k = 1, 2, ..., n-1 \\ &\frac{\partial W^p}{\partial \boldsymbol{c}_{e_r}^k} = \begin{bmatrix} \frac{1}{2} \left(\boldsymbol{\varepsilon}_{e_r}^{p^{k+1}} - \boldsymbol{\varepsilon}_{e_r}^{p^{k-1}} \right) w_r & \frac{1}{2} \left(\boldsymbol{\sigma}_{e_r}^{k-1} - \boldsymbol{\sigma}_{e_r}^{k+1} \right) w_r & 0 & 0 \end{bmatrix} \end{aligned} \tag{52}$$

Implementation of the above described sensitivity analysis is verified numerically in Appendix B.

4 Density-based RUC design

In this section, some of the issues that arise when using topology optimization to design an RUC are discussed and approaches to handle these issues are presented. For illustrating these issues, von Mises plasticity without rotation is considered, i.e., the scaling factors χ and ω are set to 1 and the angle $\theta = 0$. All of the topology optimization examples in this section and throughout the remainder of the study utilize the following settings: elastic material parameters are set to $E = 2500$ and $\nu = 0.38$ while the hardening coefficient $K^h = 125$ and is normalized by the yield stress $\sigma_y = 20$ (see (13)). RUC equilibrium (25) is solved using an adaptive step-size Newton-Raphson method (Crisfield 1991) with convergence criterion based on the global energy residual, $\text{abs}\left(\boldsymbol{R}^T \boldsymbol{\Delta}\hat{\boldsymbol{u}}\right) \leq 10^{-12}$. Optimization is performed using the Method of Moving Asymptotes (MMA) (Svanberg 1987) with default algorithmic parameters. A continuation scheme is utilized to gradually increase the penalization parameters p_0 and p_1 from values of 3 and 2.5 to values of 5 and 4.5, respectively, using an increment of 0.2 every 20 optimization iterations. Optimization is then terminated after 300 total iterations. The volume fraction used throughout is $V_f = 0.4$. Both the optimization and FEA are performed using an in-house Matlab based finite element library CPSSL-FEA developed at the University of Notre Dame.

4.1 Initial density distribution

When using a density-based design parameterization, the initial design for a given domain is usually taken as a homogeneous distribution of element density variables set to the value of the prescribed volume fraction. In this way, there is no predefined topology that could bias the optimizer toward a certain local optima. This strategy is successful in structural design as the displacement field will

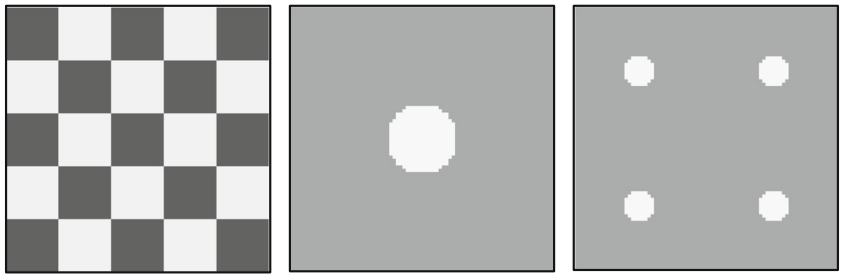

a) Checkerboard b) Centered hole c) Four holes

Fig. 2 Three initial density distributions for square RUC design domain

be non-uniform throughout the domain due to the prescribed boundary data. A non-uniform displacement field leads to non-uniform sensitivity values which are used by the optimizer to improve the density distribution, resulting eventually in an optimized design. In computational homogenization, the entire RUC domain is deformed as a whole by the macroscopic strain tensor. Thus, the displacement field is non-uniform only if the RUC contains microstructural heterogeneities. A uniform initial density distribution will correspond to a homogeneous microstructure and therefore will result in a homogeneous microscale displacement field and uniform sensitivity values. In this case, the optimizer will be unable to improve the design. In order to have non-uniform sensitivity values in the RUC domain, the initial density distribution must thus be non-uniform. However, using a non-uniform initial density distribution biases the topology towards a certain local optima dictated by the initial distribution. This is not a debilitating problem, but the designer must be cognizant of this issue. Indeed, in the level set design parameterization often used to perform topology optimization, there is also a dependence on initial design, and this has not stopped the method from being useful (van Dijk et al. 2013).

The effect of initial density distribution is illustrated through numerical studies utilizing a square RUC design domain (see RUC 2 in Fig. 1) of dimensions 1000 by 1000 discretized into an 80×80 mesh of plane strain Q1/E4 EAS elements. For this design domain, three initial density distributions are considered as shown in Fig. 2. The first initial distribution consists of a checkerboard pattern of 16×16 element squares, the second has a hole with a radius of 8 elements in the center of the RUC and the third has four holes with 5 element radii each centered in one of the four quadrants of the RUC. The contrast between density values in the initial designs also affects the sensitivity values and throughout this study, the density values in the lighter

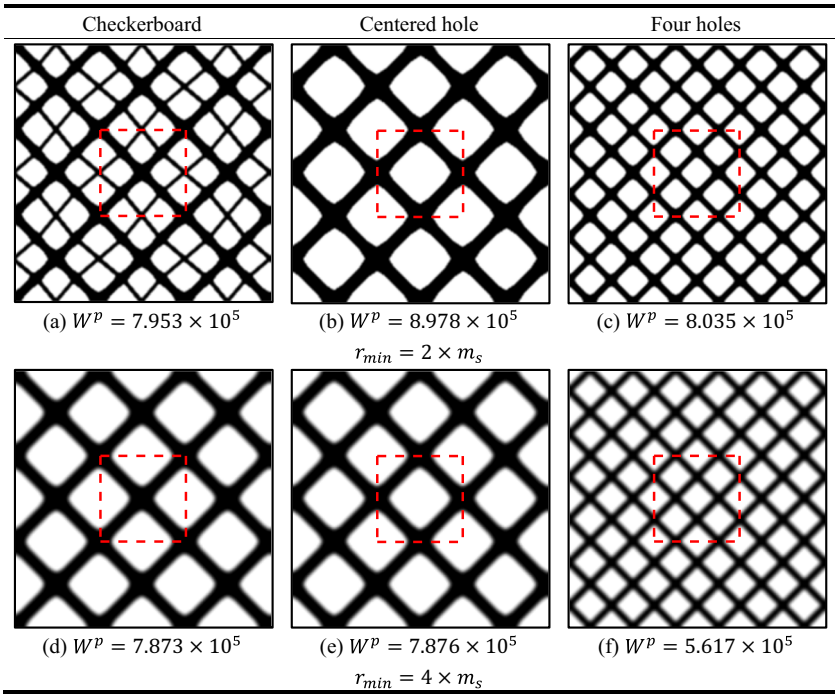

Fig. 3 Optimized microstructures obtained for von Mises plasticity under simple shear using three different initial density distributions and different filter radii

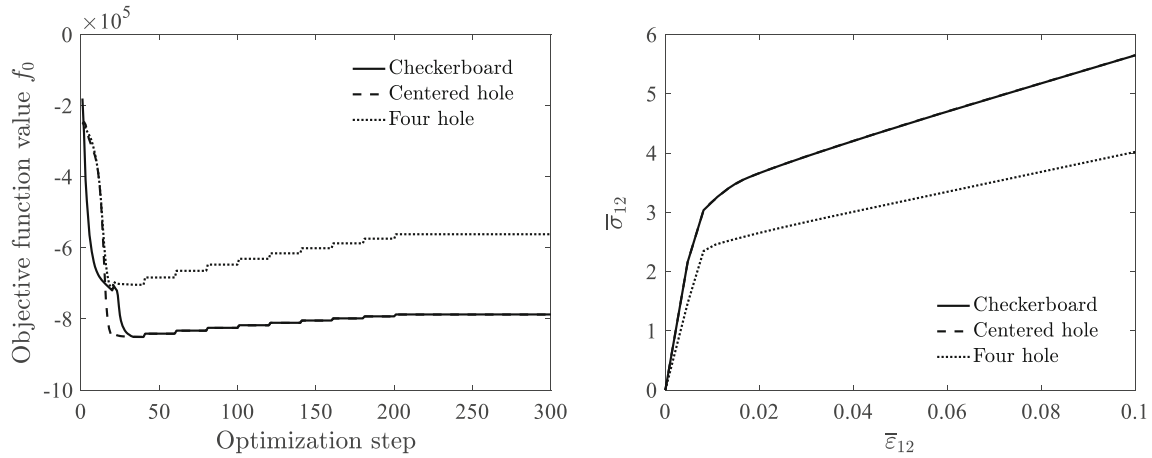

Fig. 4 Optimization convergence history and {12}-component macroscopic stress-strain response for optimized RUC topologies subject to simple shear using three different initial density distributions and $r_{min} = 4 \times m_s$

regions of the RUC shown in Fig. 2 are set to be one tenth of the values of the darker regions.

To illustrate how the initial density distribution can influence the optimized topologies obtained, the three distributions shown in Fig. 2 are used to perform topology optimization for an RUC subject to a prescribed macroscopic strain tensor $\hat{\bar{\boldsymbol{\varepsilon}}} = \begin{bmatrix} 0 & 0 & 0.2 \end{bmatrix}$, which corresponds to a simple shear deformation. Figure 3 shows the optimized microstructures obtained by using two different filter radius values. The optimized microstructures shown consist of a 3×3 array of RUCs and a red dashed line is used to outline the optimized RUC domain. The filter radii considered are $r_{min} = 2 \times m_s$ and $r_{min} = 4 \times m_s$ where m_s is the size of an element in the uniform mesh and the total plastic work in the RUC domain is also reported.

When using a filter radius $r_{min} = 2 \times m_s$, it can be seen that the optimized topologies are similar, but the topology obtained using the centered hole initial density distribution has the best performance. The optimized topology obtained using the four hole initial density distribution (Fig. 3c) unsurprisingly appears to be a 2×2 repetition of that in Fig. 3b, while the optimized topology using the checkerboard initial distribution (Fig. 3a) appears to be the same as in Fig. 3b but with additional thin cross bar features. Because the topology in Fig. 3c has smaller features in the RUC, the smearing effect of the filter is exaggerated, as there are more locations where there is an interface between solid and void elements. This, in turn, causes less total plastic work to be dissipated within the RUC due to the interpolation scheme reducing the plastic work of intermediate density elements. Hence, while the topology in Fig. 3c is a scaled down version of that in Fig. 3b, the total plastic work dissipated within the RUC is less. For a similar reason, the thinner cross bar features in Fig. 3a cause this design to be less optimal than that in Fig. 3b.

When the filter radius is increased to $r_{min} = 4 \times m_s$, the topologies obtained using the checkerboard (Fig. 3d) and centered hole (Fig. 3e) initial distributions converge, while that obtained using the four hole initial distribution (Fig. 3f) remains a scaled down version of this topology.

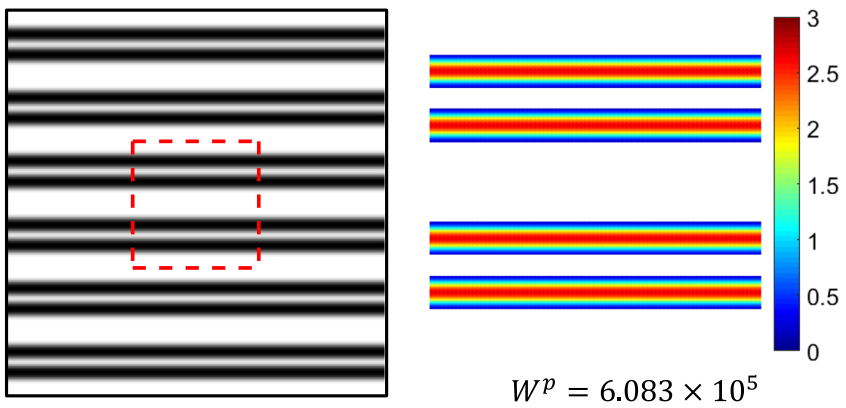

Fig. 5 Optimized microstructure and plastic work density distribution within RUC for von Mises plasticity under uniaxial compression using four hole initial density distribution

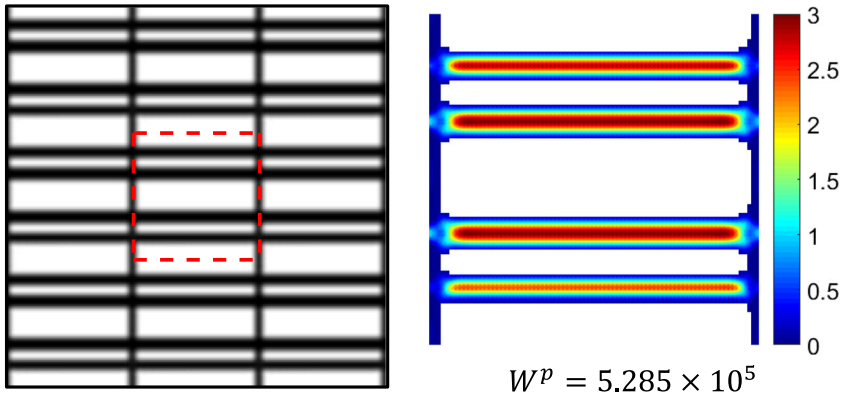

Fig. 6 Optimized microstructure and plastic work density distribution within RUC for von Mises plasticity under uniaxial compression using four hole initial density distribution with constraint on $\overline{\mathbb{C}}^0_{2222}$

Hence, by controlling feature size through the density filter, pathological issues related to the emergence of thin features which hinder the performance of the design can be reduced and the same topology can be obtained when using different initial density distributions. This convergence can be observed also in the optimization convergence history and macroscopic stress-strain response of the {12}-component shown in Fig. 4a, b, respectively. Convergence to the same design may not be the case under different macroscopic deformation modes, but a filter radius of $r_{min} = 4 \times m_s$ seems to allow unique topological features to develop while also helping to avoid less desirable local minima defined by thin features. Hence, this filter radius is employed for the remainder of the examples in Sections 4 and 5.

4.2 Microstructural connectivity

Another important issue when designing energy dissipating microstructures with voids is that of microstructural connectivity. This issue results again from the fact that RUC domain is deformed as a whole by the prescribed macroscopic strain tensor, hence the deformation is agnostic as to whether disparate regions of the domain are connected by material. For example, Fig. 5 shows the optimized microstructure obtained using the four hole initial density distribution subject to a uniaxial compression deformation mode with $\hat{\bar{\boldsymbol{\varepsilon}}} = \begin{bmatrix} -0.1 & 0 & 0 \end{bmatrix}$. While this RUC topology maximizes the use of material for energy dissipation, as seen through the even plastic work density distribution within the RUC, the resulting microstructure is not connected in the vertical direction and hence is useless. This issue may occur under different macroscopic deformation modes and thus requires a technique to remedy it.

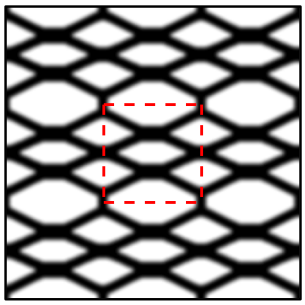

Fig. 7 Optimized microstructure for Hoffman plasticity with $\omega = 2$ and $\chi = 4$ under uniaxial compression using checkerboard initial density distribution

The connectivity issue is typically not observed in elastic microstructure design, as the objective is to optimize the elasticity tensor to obtain extremal stiffness values while maintaining different kinds of macroscopic elastic symmetry (isotropy, square symmetry, orthotropy, etc.). Hence, connectivity does not become an issue since an unconnected microstructure would have negligible entries in the elasticity tensor and thus not meet stiffness requirements. With this in mind, enforcing some sort of stiffness constraint seems like a viable way to ensure connected microstructures. Stiffness is reflected in the entries of the initial homogenized tangent moduli tensor $\overline{\mathbb{C}}^0$, i.e., the homogenized tangent moduli tensor of the RUC when in the elastic regime. To obtain $\overline{\mathbb{C}}^0$, the tangent stiffness matrix $\boldsymbol{K}_T$ in the Jacobian $\boldsymbol{J}$ of (34) is replaced with the elastic stiffness matrix $\boldsymbol{K}_E$, given as

$$\begin{aligned} \boldsymbol{K}_E &= \mathop{\mathcal{A}}_{e=1}^{n_{ele}} \boldsymbol{K}_E^e \\ \boldsymbol{K}_E^e &= \int_{\Omega^{\mu e}} \boldsymbol{B}^T \mathbb{C}^E \boldsymbol{B} dv \end{aligned} \tag{53}$$

where $\mathbb{C}^E$ is the linear elasticity tensor, assumed in this study to be isotropic at the microscale and interpolated using (35). With this in hand, constraints can be directly formulated on entries of $\overline{\mathbb{C}}^0$ to ensure stiffness in certain directions. This approach provides flexibility to the designer as constraints can be applied to individual entries of $\overline{\mathbb{C}}^0$ or to combinations of entries. For instance, to ensure

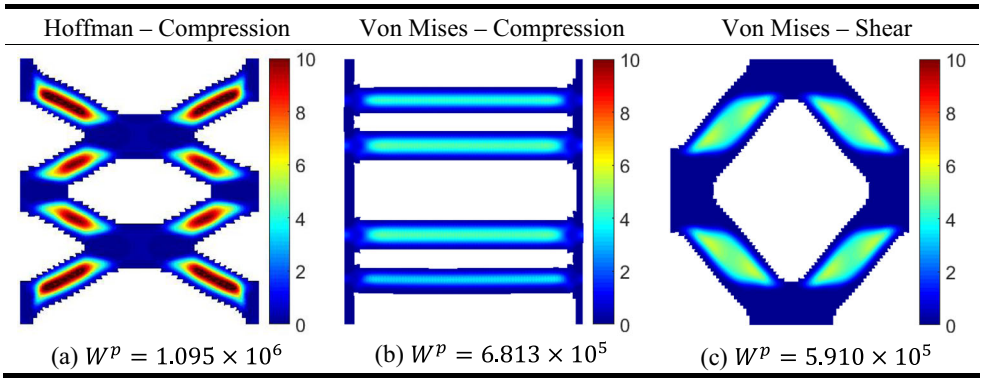

Fig. 8 Plastic work density distributions within deformed optimized RUC domains subject to uniaxial compression. Comparison between design optimized for uniaxial compression using Hoffman plasticity with $\omega = 2$ and $\chi = 4$ and designs optimized for uniaxial compression and simple shear using von Mises plasticity

connectivity under uniaxial compression, the entry $\overline{\mathbb{C}}^0_{2222}$ can be constrained to be a certain fraction of the component $\overline{\mathbb{C}}^0_{1111}$, i.e.

$$\overline{\mathbb{C}}^0_{2222} \geq a_0 \overline{\mathbb{C}}^0_{1111} \tag{54}$$

where a_0 is a prescribed ratio. Enforcing constraints of this type requires computing the sensitivity of the entries of $\overline{\mathbb{C}}^0$. The sensitivity of $\overline{\mathbb{C}}^0$ with respect to density variable ρ_j can be obtained from (34) as

$$\frac{\partial \overline{\mathbb{C}}^0}{\partial \rho_j} = -\frac{1}{V} \boldsymbol{D}^T \frac{\partial \boldsymbol{J}^{-1}}{\partial \rho_j} \boldsymbol{D} = \frac{1}{V} \boldsymbol{S}^T \frac{\partial \boldsymbol{J}}{\partial \rho_j} \boldsymbol{S} \tag{55}$$

where the matrix $\boldsymbol{S} = \boldsymbol{J}^{-1}\boldsymbol{D}$ is only computed once while the term $\partial \boldsymbol{J}/\partial \rho_j$ is computed for each element design variable as

$$\begin{aligned} \frac{\partial \boldsymbol{J}}{\partial \rho_j} &= \begin{bmatrix} \overset{n_{ele}}{\underset{e=1}{\mathcal{A}}} \left(\frac{\partial \boldsymbol{K}^e_E}{\partial \rho_j} \right) & \boldsymbol{0} \\ \boldsymbol{0} & \boldsymbol{0} \end{bmatrix} \quad \text{with} \\ \frac{\partial \boldsymbol{K}^e_E}{\partial \rho_j} &= \begin{cases} \displaystyle\int_{\Omega^{\mu e}} \boldsymbol{B}^T \frac{\partial \mathbb{C}^E}{\partial \rho_j} \boldsymbol{B} dv, & j = e \\ \boldsymbol{0}, & j \neq e \end{cases} \end{aligned} \tag{56}$$

To illustrate the enforcement of the stiffness constraint in (54), the RUC subject to uniaxial compression with four hole initial density distribution is again considered. Figure 6 shows the result of enforcing the constraint with $a_0 = 0.1$. It can be observed that the topology is well connected as minimum initial stiffness in the 2-direction is directly enforced. Moreover, plastic work is distributed in the horizontal members, as expected. Of course, this approach will also depend on the problem at hand and requires a priori knowledge of which entries of $\overline{\mathbb{C}}^0$ are needed for connectivity of a given problem. However, it provides a viable route through which microstructural connectivity can be enforced.

5 RUC designs with anisotropic plasticity

In this section, plastic anisotropy is considered using the same square RUC domain as in the previous section. Optimized topologies are compared to those obtained using von Mises plasticity in Section 4 under the same deformation modes. Additionally, optimized RUC topologies with anisotropic plastic parameters are obtained under a more complex deformation mode and with macroscopic elastic orthotropy enforced. This orthotopy is enforced by prescribing lines of geometric symmetry in the RUC domain as has been done for elastic microstructures in previous studies, e.g., Neves et al. (2000).

5.1 Uniaxial compression

The uniaxial compression case given by setting $\hat{\hat{\boldsymbol{\varepsilon}}} = \begin{bmatrix} -0.1 & 0 & 0 \end{bmatrix}$ and optimized using von Mises plasticity in Section 4.2 is now considered with plastic anisotropy. The scaling parameters ω and χ are set to 2 and 4, respectively. Results are obtained using the checkerboard initial density distribution and Fig. 7 shows the optimized microstructure with RUC outlined by red dashed lines.

It is immediately obvious that this optimized microstructure is quite different from that in Fig. 5, as it is well connected without needing any constraints. This is caused

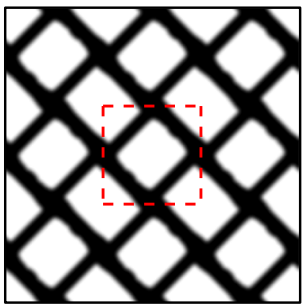

Fig. 9 Optimized microstructure for Hoffman plasticity with $\omega = 2$, $\chi = 2$ and $\theta = \pi/4$ under simple shear using centered hole initial density distribution

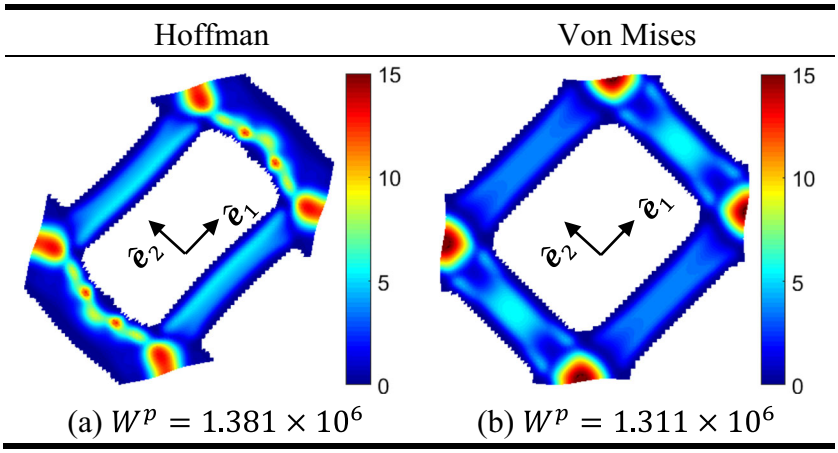

Fig. 10 Plastic work density distributions within deformed optimized RUC domains subject to simple shear. Comparison between design optimized for simple shear using Hoffman plasticity with $\omega = 2$, $\chi = 2$ and $\theta = \pi/4$ and design optimized for simple shear using von Mises plasticity

by the anisotropic scaling factors χ and ω which increase the values of initial yield stresses $\hat{\sigma}^t_{11}$ and $\hat{\sigma}^c_{11}$. While this makes yielding more difficult to initiate, it also means that the plastic work done after yielding is greater due to the high yield stresses. Hence, the topology evolves so as to exploit this phenomenon, which can be seen in the distribution of plastic work density within the deformed optimized RUC domain in Fig. 8a. Also shown in Fig. 8 is the distribution of plastic work density within the RUCs optimized for uniaxial compression (i.e., the topology from Fig. 6) and simple shear (i.e., the topology in Fig. 3e) using von Mises plasticity and analyzed using Hoffman plasticity with $\omega = 2$ and $\chi = 4$.

From the total plastic work values reported in Fig. 8, it can be seen that the topology optimized for uniaxial compression using Hoffman plasticity with $\omega = 2$ and $\chi = 4$ (Fig. 8a) performs significantly better than the other two topologies (Fig. 8b, c). The reason for this is the parameters $\omega = 2$ and $\chi = 4$ which cause the value of the yield stress $\hat{\sigma}^c_{11}$ to be large. This makes yielding more difficult in members which are oriented so as to be compressed along this direction, as can be observed in the horizontal members of Figure 8b. Thus, orienting the members so that they are compressed at an angle allows for more yielding to occur, which is seen in the higher plastic work density values in Fig. 8a. However, orienting the members at too great an angle can cause them to deform such that these members experience less compression, resulting in less plastic work. This is seen in Fig. 8c. Hence, the topology shown in Fig. 7 has evolved so as to exploit the physics of the problem, demonstrating that this physics is well captured during the optimization process.

5.2 Simple shear

Next, the simple shear deformation mode defined by $\hat{\bar{\boldsymbol{\varepsilon}}} = \begin{bmatrix} 0 & 0 & 0.2 \end{bmatrix}$ and optimized using von Mises plasticity in Section 4.1 is again considered. Plastic anisotropy is simulated by setting the Hoffman model parameters to $\omega = 2$, $\chi = 2$ and $\theta = \pi/4$, and the optimized microstructure obtained using the centered hole initial density distribution is shown in Fig. 9.

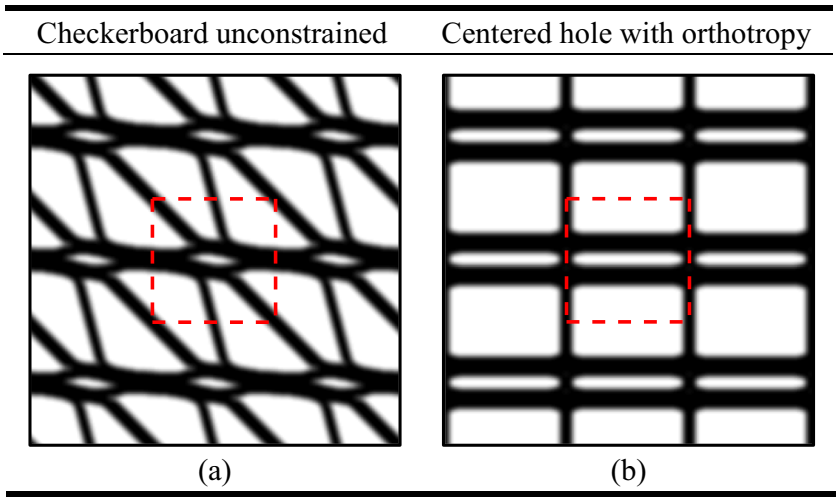

Fig. 11 Optimized microstructures for Hoffman plasticity with $\omega = 2$, $\chi = 1$ and $\theta = 0$ under combined compression and shear using checkerboard initial density distribution and centered hole initial density distribution with elastic orthotropy enforced

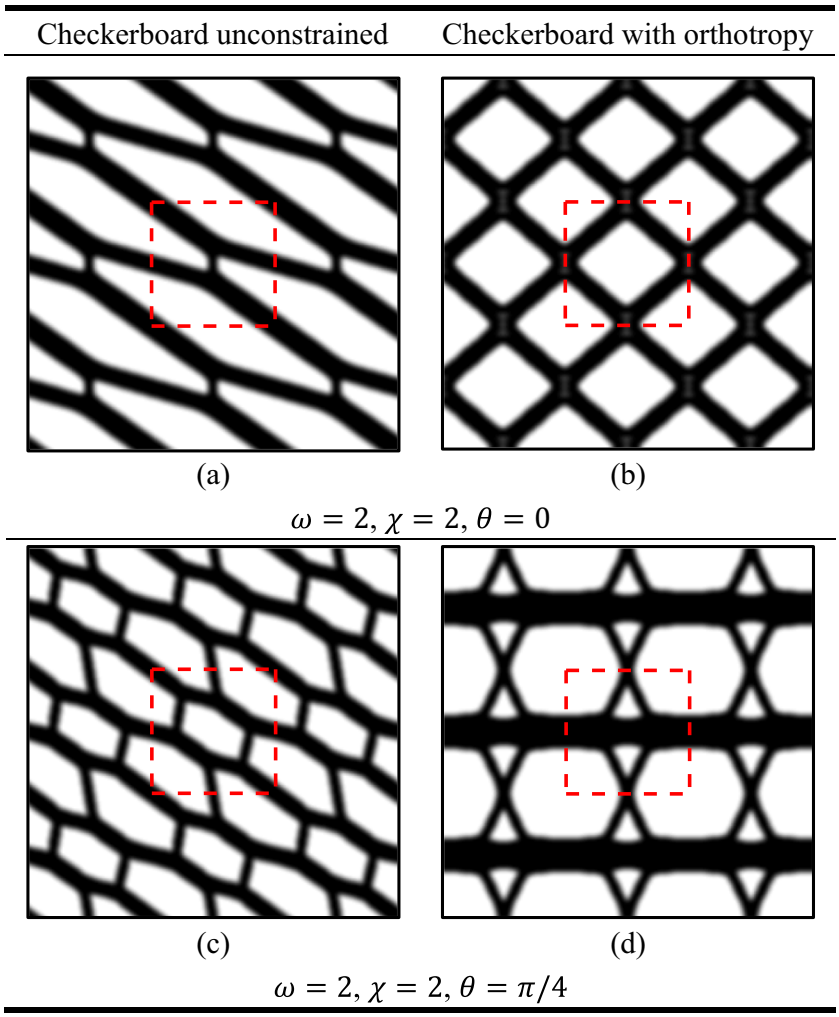

Fig. 12 Optimized microstructures for Hoffman plasticity with different parameters under combined compression and shear using checkerboard initial density distribution with and without elastic orthotropy enforced

Comparison with Fig. 3e reveals that a different design is obtained when anisotropy is considered, most noticeable in the lack of symmetry of the angled members. In the optimized topology of Fig. 9, the members going from the upper left corner to the lower right corner are thicker than the members going from the upper right corner to the lower left corner. Moreover, these members are alternatingly staggered at their intersections. While these differences are somewhat subtle, they have a large impact on the deformation of the RUC and the resulting plastic work. This can be better understood by looking at the deformed RUC domain and the plastic work density distribution therein,

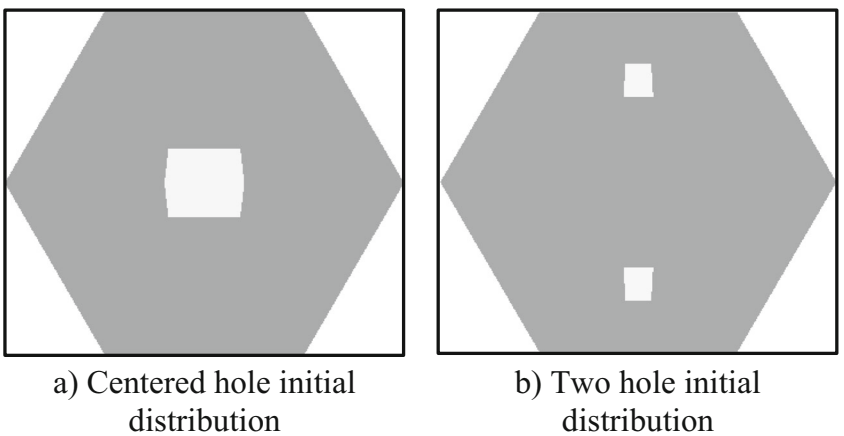

Fig. 13 Two initial density distributions for hexagonal RUC design domain

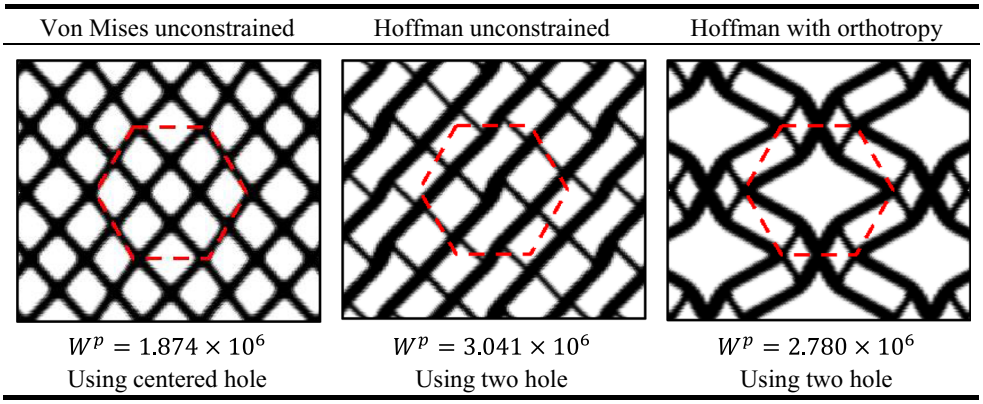

Fig. 14 Optimized microstructures for three cases using a hexagonal RUC domain under simple shear.

which is shown in Fig. 10a. It is clear that this topology experiences bending deformations caused by the staggering of the angled members and that much of the plastic work is distributed in regions experiencing this bending. Compare this to the RUC optimized for simple shear using von Mises plasticity (i.e. the topology from Fig. 3e) which is analyzed using $\omega = 2$, $\chi = 2$ and $\theta = \pi/4$ and shown in Fig. 10b. Clearly, this topology experiences less bending, which negatively affects its performance as indicated by the total plastic work values reported in Fig. 10.

Again, the reason for these differences can be attributed to the Hoffman parameters ω, χ and θ. As discussed in Section 5.1, the parameters ω and χ cause the value of the yield stress $\hat{\sigma}^c_{11}$ to be large. However, because of θ the basis $\{\hat{\boldsymbol{e}}_1, \hat{\boldsymbol{e}}_2, \hat{\boldsymbol{e}}_3\}$ along which the yield stresses are defined is no longer aligned with the global Euclidean basis $\{\boldsymbol{e}_1, \boldsymbol{e}_2, \boldsymbol{e}_3\}$. Instead, $\hat{\boldsymbol{e}}_1$ and $\hat{\boldsymbol{e}}_2$ are rotated by an angle of $\pi/4$ in plane (see the illustration of these basis vectors in Fig. 10). Thus, the applied shear deformation causes members aligned with $\hat{\boldsymbol{e}}_1$ to experience tension while members aligned with $\hat{\boldsymbol{e}}_2$ experience compression. In Fig. 10b, the members aligned with $\hat{\boldsymbol{e}}_2$ are able to yield more easily than those aligned with $\hat{\boldsymbol{e}}_1$ because of the increased tensile and compressive yield stresses along $\hat{\boldsymbol{e}}_1$ being scaled by χ. In Fig. 10a, the same effect is present, but the members experience bending in addition to axial deformations, which increases the plastic work in these members. In both cases, there is high plastic work at the intersections between members due to the interactions of stresses at these locations. This example further illustrates how the physics of the problem is accounted for during optimization to produce optimized topologies that can effectively exploit it.

5.3 Combined compression and shear

The optimized RUC topologies obtained thus far have been subject to simple deformation modes, i.e., simple shear or uniaxial compression. In this section, a more complex deformation mode combining compression and shear is applied to the RUC and different anisotropic plastic parameters are considered. The deformation mode is defined by the macroscopic strain tensor $\hat{\bar{\boldsymbol{\varepsilon}}} = \begin{bmatrix} -0.06 & -0.04 & 0.04 \end{bmatrix}$ and the Hoffman model parameters are first set to $\omega = 2$, $\chi = 1$ and $\theta = 0$. The optimized microstructure obtained using the checkerboard initial density distribution is shown in Fig. 11a.

It can be seen that this microstructure is well connected but is not as ordered as the microstructures obtained previously. In order to obtain a more ordered microstructure, the same deformation mode and anisotropic parameters are considered, but macroscopic elastic orthotropy is enforced. The optimized microstructure obtained in this case using the centered hole initial density distribution is shown in Fig. 11b where it can be seen that this microstructure is much more well-ordered. Next, the scaling factor ω is kept at a value of 2 while the scaling factor χ is set to 2 and two values of the angle θ, 0 and $\pi/4$, are considered. The optimized microstructures obtained for these cases using the checkerboard initial density distribution with and without macroscopic elastic orthotropy are shown in Fig. 12. Comparing these topologies to those in Fig. 11 illustrates how different anisotropic parameters can substantially affect the optimized microstructural designs and how enforcement of macroscopic elastic symmetry provides a way to control the order and symmetry of these microstructures.

6 Hexagonal RUC design

To illustrate how a different RUC domain can be canonically incorporated within the design framework presented herein, a hexagonal RUC design domain (see RUC 1 in Fig. 1) is considered for topology optimization. Each side of the hexagonal domain has a dimension of 1000 and 6400 non-uniform Q1/E4 EAS elements are used for discretization. The filter radius used for topology optimization with this RUC design domain is set to 50 and two different initial density distributions are considered, as shown in Fig. 13a

and b. The first distribution consists of a square hole with side length of 16 elements while the second consists of two square holes with side length of 8 elements centered in the top and bottom half of the domain. The lighter regions of the RUCs in Fig. 13a, b contain density values which are one tenth of the density values in the darker regions.

This RUC is subject to a simple shear deformation mode, again with $\hat{\hat{\boldsymbol{\varepsilon}}} = \begin{bmatrix} 0 & 0 & 0.2 \end{bmatrix}$. For each of the two initial density distributions, three different cases are considered. In the first case the Hoffman model parameters are set to $\omega = 1$, $\chi = 1$ and $\theta = 0$ to recover von Mises plasticity, while in the second case the Hoffman model parameters are set to $\omega = 4$, $\chi = 2$ and $\theta = \pi/4$. In the third case, the Hoffman parameters are again $\omega = 4$, $\chi = 2$ and $\theta = \pi/4$ and macroscale elastic orthotropy is enforced by prescribing geometric lines of symmetry. The best performing optimized microstructure obtained from the two initial density distributions is shown in Fig. 14 for each case, with the optimized RUCs outlined by red dashed lines. The microstructures obtained in this case are significantly different from those obtained with square RUCs. This example demonstrates how different RUC design domains can be chosen to obtain optimized microstructures.

7 Conclusions

In this study, topology optimization is used to design periodic elastoplastic microstructures for the purpose of energy dissipation. The combination of an RVE-based multiscale model for computational homogenization and a density-based design parameterization allows for a consistent handling of material nonlinearities from both the analysis and design update perspectives. While optimized topologies are sensitive to the choice of initial density distribution, this can be mitigated through appropriate use of the density filter. Additionally, certain problems may produce optimized microstructural topologies which are unconnected. A strategy to remedy this issue is presented and shown to result in discrete and well-connected optimized RUC topologies. The Hoffman plasticity model is used to simulate the plastic anisotropy which may be present in microstructures fabricated using additive manufacturing techniques, and it is demonstrated how this anisotropy leads to optimized RUC topologies which differ from those obtained using isotropic von Mises plasticity. Moreover, both square and hexagonal RUC design domains are utilized to obtain optimized microstructures.

The techniques laid out in this study provide a foundation for investigating the design of material microstructures with inelastic behavior using topology optimization. In this regard, there is a significant amount of work that can be done to improve upon and extend these techniques. For one, multi-material design parameterizations can be included to design inelastic microstructural composites. Additionally, extension to the finite deformation regime is desirable for designing microstructures under more realistic deformation modes. Finally, due to the computational burden of solving coupled nonlinear multiscale problems, extension to concurrent multiscale design appears to be a significant challenge and will require innovative approaches.

Funding information The presented work is supported in part by the US National Science Foundation through Grant CMMI-1762277. Any opinions, findings, conclusions, and recommendations expressed in this paper are those of the authors and do not necessarily reflect the views of the sponsors.

Appendix A: Sensitivity derivatives for Hoffman model

This appendix presents the derivatives needed for sensitivity analysis using the Hoffman plasticity model which were

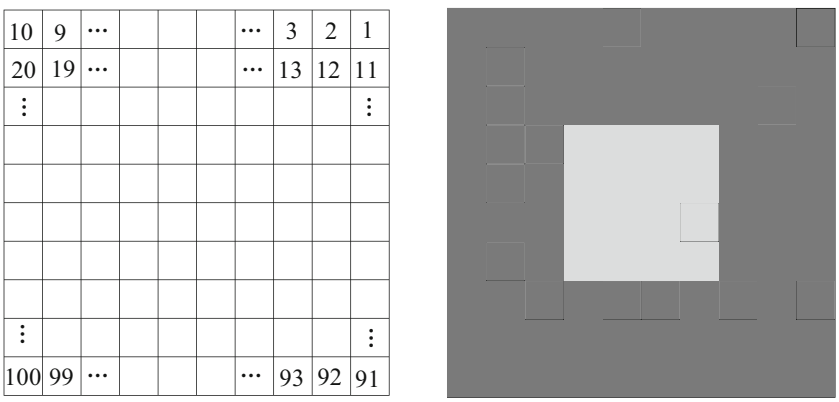

Fig. 15 Square RUC domain with element numbering and density distribution

originally derived in Ref. Zhang et al. (2017). These derivatives are based on the discrete form of the evolution equations which come from the numerical implementation using an elastic predictor/plastic return-mapping algorithm. As this implementation has been detailed in prior studies (De Borst and Feenstra 1990; Schellekens and De Borst 1990; De Souza Neto et al. 2011), it is not presented herein. Interested readers are directed to Appendix A in Zhang et al. (2017) for details on the elastic predictor/plastic return-mapping algorithm.

For the choice of $\boldsymbol{c}^k$ shown in (45), the corresponding local constraint set $\boldsymbol{H}^k$ is

$$\boldsymbol{H}^k = \begin{bmatrix} \boldsymbol{H}_1^k \\ \vdots \\ \boldsymbol{H}_{n_{ele}}^k \end{bmatrix} = \boldsymbol{0} \quad \text{with} \quad \boldsymbol{H}_e^k = \begin{bmatrix} \boldsymbol{H}_{e_1}^k \\ \boldsymbol{H}_{e_2}^k \\ \boldsymbol{H}_{e_3}^k \\ \boldsymbol{H}_{e_4}^k \\ \tilde{\boldsymbol{H}}_e^k \end{bmatrix} \tag{57}$$

Here,

$$\tilde{\boldsymbol{H}}_e^k = \sum_{r=1}^{n_{ipt}} \boldsymbol{G}_{e_r}^T \boldsymbol{\sigma}_{e_r}^k w_r = \boldsymbol{0} \tag{58}$$

and for an elastic step

$$\boldsymbol{H}_{e_r}^k = \begin{cases} \boldsymbol{h}_{e_r1}^k = \hat{\boldsymbol{\sigma}}_{e_r}^k - \hat{\boldsymbol{C}}^e \left(\hat{\boldsymbol{\varepsilon}}_{e_r}^k - \hat{\boldsymbol{\varepsilon}}_{e_r}^{p^k} \right) = \boldsymbol{0} \\ \boldsymbol{h}_{e_r2}^k = \hat{\boldsymbol{\varepsilon}}_{e_r}^{p^k} - \hat{\boldsymbol{\varepsilon}}_{e_r}^{p^{k-1}} = \boldsymbol{0} \\ h_{e_r3}^k = \alpha_{e_r}^k - \alpha_{e_r}^{k-1} = 0 \\ h_{e_r4}^k = \Delta\gamma_{e_r}^k = 0 \end{cases} \tag{59}$$

while for a plastic step

$$\boldsymbol{H}_{e_r}^k = \begin{cases} \boldsymbol{h}_{e_r1}^k = \hat{\boldsymbol{\sigma}}_{e_r}^k - \hat{\boldsymbol{C}}^e \left(\hat{\boldsymbol{\varepsilon}}_{e_r}^k - \hat{\boldsymbol{\varepsilon}}_{e_r}^{p^k} \right) = \boldsymbol{0} \\ \boldsymbol{h}_{e_r2}^k = \hat{\boldsymbol{\varepsilon}}_{e_r}^{p^k} - \hat{\boldsymbol{\varepsilon}}_{e_r}^{p^{k-1}} - \Delta\gamma_{e_r}^k \left(\boldsymbol{P}\hat{\boldsymbol{\sigma}}_{e_r}^k + \boldsymbol{q} \right) = \boldsymbol{0} \\ h_{e_r3}^k = \alpha_{e_r}^k - \alpha_{e_r}^{k-1} - \sqrt{\frac{2z_{e_r}^k}{3}} \Delta\gamma_{e_r}^k = 0 \\ h_{e_r4}^k = \frac{1}{2} \hat{\boldsymbol{\sigma}}_{e_r}^{k^T} \boldsymbol{P} \hat{\boldsymbol{\sigma}}_{e_r}^k + \boldsymbol{q}^T \hat{\boldsymbol{\sigma}}_{e_r}^k - \zeta^2(\alpha_{e_r}^k) = 0 \end{cases} \tag{60}$$

with $z_{e_r}^k = \left(\boldsymbol{P}\hat{\boldsymbol{\sigma}}_{e_r}^k + \boldsymbol{q} \right)^T \boldsymbol{Z} \left(\boldsymbol{P}\hat{\boldsymbol{\sigma}}_{e_r}^k + \boldsymbol{q} \right)$.
The derivative $\partial \boldsymbol{H}^k / \partial \boldsymbol{u}^{k-1} = \boldsymbol{0}$ while

$$\frac{\partial \boldsymbol{H}^k}{\partial \boldsymbol{u}^k} = \begin{bmatrix} \dfrac{\partial \boldsymbol{H}_1^k}{\partial \boldsymbol{u}^k} \\ \vdots \\ \dfrac{\partial \boldsymbol{H}_{n_{ele}}^k}{\partial \boldsymbol{u}^k} \end{bmatrix} \text{ with}$$

$$\frac{\partial \boldsymbol{H}_j^k}{\partial \boldsymbol{u}^k} = \mathop{\mathcal{A}}_{e=1}^{n_{ele}} \left(\frac{\partial \boldsymbol{H}_j^k}{\partial \boldsymbol{u}_e^k} \right), \quad j = 1, 2, ..., n_{ele} \tag{61}$$

The terms $\partial \boldsymbol{H}_j^k / \partial \boldsymbol{u}_e^k$ are nonzero only when $j = e$ and are calculated as

$$\frac{\partial \boldsymbol{H}_e^k}{\partial \boldsymbol{u}_e^k} = \begin{bmatrix} \dfrac{\partial \boldsymbol{H}_{e_1}^k}{\partial \boldsymbol{u}_e^k} & \dfrac{\partial \boldsymbol{H}_{e_2}^k}{\partial \boldsymbol{u}_e^k} & \dfrac{\partial \boldsymbol{H}_{e_3}^k}{\partial \boldsymbol{u}_e^k} & \dfrac{\partial \boldsymbol{H}_{e_4}^k}{\partial \boldsymbol{u}_e^k} & \dfrac{\partial \tilde{\boldsymbol{H}}_e^k}{\partial \boldsymbol{u}_e^k} \end{bmatrix}^T$$

$$\frac{\partial \boldsymbol{H}_{e_r}^k}{\partial \boldsymbol{u}_e^k} = \begin{bmatrix} -\hat{\boldsymbol{C}}^e \boldsymbol{T}_2 \boldsymbol{B}_r \\ \boldsymbol{0} \\ \boldsymbol{0} \\ \boldsymbol{0} \end{bmatrix} \quad \text{and} \quad \frac{\partial \tilde{\boldsymbol{H}}_e^k}{\partial \boldsymbol{u}_e^k} = \boldsymbol{0} \tag{62}$$

The derivatives $\partial \boldsymbol{H}^k / \partial \boldsymbol{c}^k$ and $\partial \boldsymbol{H}^k / \partial \boldsymbol{c}^{k-1}$ have the same structure, i.e.

$$\frac{\partial \boldsymbol{H}^k}{\partial \boldsymbol{c}^k} = \begin{bmatrix} \dfrac{\partial \boldsymbol{H}_1^k}{\partial \boldsymbol{c}_1^k} & \boldsymbol{0} & \dots & \boldsymbol{0} \\ \boldsymbol{0} & \dfrac{\partial \boldsymbol{H}_2^k}{\partial \boldsymbol{c}_2^k} & \dots & \boldsymbol{0} \\ \vdots & \vdots & \ddots & \vdots \\ \boldsymbol{0} & \boldsymbol{0} & \dots & \dfrac{\partial \boldsymbol{H}_{n_{ele}}^k}{\partial \boldsymbol{c}_{n_{ele}}^k} \end{bmatrix}$$

$$\frac{\partial \boldsymbol{H}^k}{\partial \boldsymbol{c}^{k-1}} = \begin{bmatrix} \dfrac{\partial \boldsymbol{H}_1^k}{\partial \boldsymbol{c}_1^{k-1}} & \boldsymbol{0} & \dots & \boldsymbol{0} \\ \boldsymbol{0} & \dfrac{\partial \boldsymbol{H}_2^k}{\partial \boldsymbol{c}_2^{k-1}} & \dots & \boldsymbol{0} \\ \vdots & \vdots & \ddots & \vdots \\ \boldsymbol{0} & \boldsymbol{0} & \dots & \dfrac{\partial \boldsymbol{H}_{n_{ele}}^k}{\partial \boldsymbol{c}_{n_{ele}}^{k-1}} \end{bmatrix} \tag{63}$$

since $\boldsymbol{c}_i^k$ and $\boldsymbol{c}_j^k$ are independent and $\boldsymbol{H}_i^k$ and $\boldsymbol{H}_j^k$ are uncoupled when $i \neq j$. The nonzero sub-matrices have the form

$$\frac{\partial \boldsymbol{H}_e^k}{\partial \boldsymbol{c}_e^k} = \begin{bmatrix} \dfrac{\partial \boldsymbol{H}_{e_1}^k}{\partial \boldsymbol{c}_{e_1}^k} & \boldsymbol{0} & \boldsymbol{0} & \boldsymbol{0} & \dfrac{\partial \boldsymbol{H}_{e_1}^k}{\partial \tilde{\boldsymbol{\alpha}}_e^k} \\ \boldsymbol{0} & \dfrac{\partial \boldsymbol{H}_{e_2}^k}{\partial \boldsymbol{c}_{e_2}^k} & \boldsymbol{0} & \boldsymbol{0} & \dfrac{\partial \boldsymbol{H}_{e_2}^k}{\partial \tilde{\boldsymbol{\alpha}}_e^k} \\ \boldsymbol{0} & \boldsymbol{0} & \dfrac{\partial \boldsymbol{H}_{e_3}^k}{\partial \boldsymbol{c}_{e_3}^k} & \boldsymbol{0} & \dfrac{\partial \boldsymbol{H}_{e_3}^k}{\partial \tilde{\boldsymbol{\alpha}}_e^k} \\ \boldsymbol{0} & \boldsymbol{0} & \boldsymbol{0} & \dfrac{\partial \boldsymbol{H}_{e_4}^k}{\partial \boldsymbol{c}_{e_4}^k} & \dfrac{\partial \boldsymbol{H}_{e_4}^k}{\partial \tilde{\boldsymbol{\alpha}}_e^k} \\ \dfrac{\partial \tilde{\boldsymbol{H}}_e^k}{\partial \boldsymbol{c}_{e_1}^k} & \dfrac{\partial \tilde{\boldsymbol{H}}_e^k}{\partial \boldsymbol{c}_{e_2}^k} & \dfrac{\partial \tilde{\boldsymbol{H}}_e^k}{\partial \boldsymbol{c}_{e_3}^k} & \dfrac{\partial \tilde{\boldsymbol{H}}_e^k}{\partial \boldsymbol{c}_{e_4}^k} & \boldsymbol{0} \end{bmatrix}$$

$$\frac{\partial \boldsymbol{H}_e^k}{\partial \boldsymbol{c}_e^{k-1}} = \begin{bmatrix} \frac{\partial \boldsymbol{H}_{e_1}^k}{\partial \boldsymbol{c}_{e_1}^{k-1}} & \mathbf{0} & \mathbf{0} & \mathbf{0} & \frac{\partial \boldsymbol{H}_{e_1}^k}{\partial \tilde{\boldsymbol{\alpha}}_e^{k-1}} \\ \mathbf{0} & \frac{\partial \boldsymbol{H}_{e_2}^k}{\partial \boldsymbol{c}_{e_2}^{k-1}} & \mathbf{0} & \mathbf{0} & \frac{\partial \boldsymbol{H}_{e_2}^k}{\partial \tilde{\boldsymbol{\alpha}}_e^{k-1}} \\ \mathbf{0} & \mathbf{0} & \frac{\partial \boldsymbol{H}_{e_3}^k}{\partial \boldsymbol{c}_{e_3}^{k-1}} & \mathbf{0} & \frac{\partial \boldsymbol{H}_{e_3}^k}{\partial \tilde{\boldsymbol{\alpha}}_e^{k-1}} \\ \mathbf{0} & \mathbf{0} & \mathbf{0} & \frac{\partial \boldsymbol{H}_{e_4}^k}{\partial \boldsymbol{c}_{e_4}^{k-1}} & \frac{\partial \boldsymbol{H}_{e_4}^k}{\partial \tilde{\boldsymbol{\alpha}}_e^{k-1}} \\ \frac{\partial \tilde{\boldsymbol{H}}_e^k}{\partial \boldsymbol{c}_{e_1}^{k-1}} & \frac{\partial \tilde{\boldsymbol{H}}_e^k}{\partial \boldsymbol{c}_{e_2}^{k-1}} & \frac{\partial \tilde{\boldsymbol{H}}_e^k}{\partial \boldsymbol{c}_{e_3}^{k-1}} & \frac{\partial \tilde{\boldsymbol{H}}_e^k}{\partial \boldsymbol{c}_{e_4}^{k-1}} & \mathbf{0} \end{bmatrix} \tag{64}$$

The terms in $\partial \boldsymbol{H}_e^k / \partial \boldsymbol{c}_{e_1}^{k-1}$ are the same for both elastic and plastic steps, i.e.

$$\frac{\partial \boldsymbol{H}_{e_r}^k}{\partial \boldsymbol{c}_{e_r}^{k-1}} = \begin{bmatrix} \mathbf{0} & \mathbf{0} & \mathbf{0} & \mathbf{0} \\ \mathbf{0} & -\boldsymbol{T}_2 & \mathbf{0} & \mathbf{0} \\ \mathbf{0} & \mathbf{0} & -1 & 0 \\ \mathbf{0} & \mathbf{0} & 0 & 0 \end{bmatrix}, \quad \frac{\partial \boldsymbol{H}_{e_r}^k}{\partial \tilde{\boldsymbol{\alpha}}_e^{k-1}} = \mathbf{0}, \quad \frac{\partial \tilde{\boldsymbol{H}}_e^k}{\partial \boldsymbol{c}_{e_r}^{k-1}} = \mathbf{0} \tag{65}$$

The terms $\partial \boldsymbol{H}_{e_r}^k / \partial \tilde{\boldsymbol{\alpha}}_e^k$ and $\partial \tilde{\boldsymbol{H}}_e^k / \partial \boldsymbol{c}_{e_r}^k$ in $\partial \boldsymbol{H}_e^k / \partial \boldsymbol{c}_e^k$ are

$$\frac{\partial \boldsymbol{H}_{e_r}^k}{\partial \tilde{\boldsymbol{\alpha}}_e^k} = \begin{bmatrix} -\hat{\boldsymbol{C}}^e \boldsymbol{T}_2 \boldsymbol{G}_{e_r} \\ \mathbf{0} \\ 0 \\ 0 \end{bmatrix}, \quad \frac{\partial \tilde{\boldsymbol{H}}_e^k}{\partial \boldsymbol{c}_{e_r}^k} = \begin{bmatrix} w_r \boldsymbol{G}_{e_r}^T & \mathbf{0} & \mathbf{0} & \mathbf{0} \end{bmatrix} \tag{66}$$

regardless of whether the step is elastic or plastic. Finally, the term $\partial \boldsymbol{H}_{e_r}^k / \partial \boldsymbol{c}_{e_r}^k$ at an elastic step is

$$\frac{\partial \boldsymbol{H}_{e_r}^k}{\partial \boldsymbol{c}_{e_r}^k} = \begin{bmatrix} \boldsymbol{T}_1 & \hat{\boldsymbol{C}}^e \boldsymbol{T}_2 & \mathbf{0} & \mathbf{0} \\ \mathbf{0} & \boldsymbol{T}_2 & \mathbf{0} & \mathbf{0} \\ \mathbf{0} & \mathbf{0} & 1 & 0 \\ \mathbf{0} & \mathbf{0} & 0 & 1 \end{bmatrix} \tag{67}$$

and at a plastic step is

$$\frac{\partial \boldsymbol{H}_{e_r}^k}{\partial \boldsymbol{c}_{e_r}^k} = \begin{bmatrix} \boldsymbol{M}_{11} & \boldsymbol{M}_{12} & \boldsymbol{M}_{13} & \boldsymbol{M}_{14} \\ \boldsymbol{M}_{21} & \boldsymbol{M}_{22} & \boldsymbol{M}_{23} & \boldsymbol{M}_{24} \\ \boldsymbol{M}_{31} & \boldsymbol{M}_{32} & \boldsymbol{M}_{33} & \boldsymbol{M}_{34} \\ \boldsymbol{M}_{41} & \boldsymbol{M}_{42} & \boldsymbol{M}_{43} & \boldsymbol{M}_{44} \end{bmatrix}$$

$$\boldsymbol{M}_{11} = \boldsymbol{T}_1, \quad \boldsymbol{M}_{12} = \hat{\boldsymbol{C}}^e \boldsymbol{T}_2, \quad \boldsymbol{M}_{13} = \mathbf{0}, \quad \boldsymbol{M}_{14} = \mathbf{0}$$

$$\boldsymbol{M}_{21} = -\Delta\gamma_{e_r}^k \boldsymbol{P} \boldsymbol{T}_1, \ \boldsymbol{M}_{22} = \boldsymbol{T}_2, \ \boldsymbol{M}_{23} = \mathbf{0}, \ \boldsymbol{M}_{24} = -\left(\boldsymbol{P}\hat{\boldsymbol{\sigma}}_{e_r}^k + \boldsymbol{q}\right)$$

$$\boldsymbol{M}_{31} = -\sqrt{\frac{1}{6z_{e_r}^k}} \Delta\gamma_{e_r}^k \frac{dz_{e_r}^k}{d\hat{\boldsymbol{\sigma}}_{e_r}^k} \boldsymbol{T}_1, \ \boldsymbol{M}_{32} = \mathbf{0}, \ M_{33} = 1, \ M_{34} = -\sqrt{\frac{2z_{e_r}^k}{3}}$$

$$\boldsymbol{M}_{41} = \hat{\boldsymbol{\sigma}}_{e_r}^{k^T} \boldsymbol{P} \boldsymbol{T}_1 + \boldsymbol{q}^T \boldsymbol{T}_1, \ \boldsymbol{M}_{42} = \mathbf{0}, \ M_{43} = -2\zeta \left(\alpha_{e_r}^k\right) \frac{d\zeta}{d\alpha_{e_r}^k}, \ M_{44} = 0 \tag{68}$$

The derivative with respect to the element density variables is

$$\frac{\partial \boldsymbol{H}^k}{\partial \boldsymbol{\rho}} = \begin{bmatrix} \frac{\partial \boldsymbol{H}_1^k}{\partial \rho_1} & \mathbf{0} & \dots & \mathbf{0} \\ \mathbf{0} & \frac{\partial \boldsymbol{H}_2^k}{\partial \rho_2} & \dots & \mathbf{0} \\ \vdots & \vdots & \ddots & \vdots \\ \mathbf{0} & \mathbf{0} & \dots & \frac{\partial \boldsymbol{H}_{n_{ele}}^k}{\partial \rho_{n_{ele}}} \end{bmatrix} \tag{69}$$

The nonzero entries $\partial \boldsymbol{H}_e^k / \partial \rho_e$ are

$$\frac{\partial \boldsymbol{H}_e^k}{\partial \rho_e} = \begin{bmatrix} \frac{\partial \boldsymbol{H}_{e_1}^k}{\partial \rho_e} & \frac{\partial \boldsymbol{H}_{e_2}^k}{\partial \rho_e} & \frac{\partial \boldsymbol{H}_{e_3}^k}{\partial \rho_e} & \frac{\partial \boldsymbol{H}_{e_4}^k}{\partial \rho_e} & \frac{\partial \tilde{\boldsymbol{H}}_e^k}{\partial \rho_e} \end{bmatrix}$$

$$\frac{\partial \tilde{\boldsymbol{H}}_e^k}{\partial \rho_e} = \mathbf{0} \tag{70}$$

For an elastic step, $\partial \boldsymbol{H}_{e_r}^k / \partial \rho_e$ is

$$\frac{\partial \boldsymbol{H}_{e_r}^k}{\partial \rho_e} = \begin{bmatrix} -\frac{\partial \hat{\boldsymbol{C}}^e}{\partial \rho_e} \left(\hat{\boldsymbol{\varepsilon}}_{e_r}^k - \hat{\boldsymbol{\varepsilon}}_{e_r}^{p^k}\right) \\ \mathbf{0} \\ 0 \\ 0 \end{bmatrix} \tag{71}$$

and for a plastic step it is

$$\frac{\partial \boldsymbol{H}_{e_r}^k}{\partial \rho_e} = \begin{bmatrix} -\frac{\partial \hat{\boldsymbol{C}}^e}{\partial \rho_e} \left(\hat{\boldsymbol{\varepsilon}}_{e_r}^k - \hat{\boldsymbol{\varepsilon}}_{e_r}^{p^k}\right) \\ -\Delta\gamma_{e_r}^k \left(\frac{\partial \boldsymbol{P}}{\partial \rho_e} \hat{\boldsymbol{\sigma}}_{e_r}^k + \frac{\partial \boldsymbol{q}}{\partial \rho_e}\right) \\ -\sqrt{\frac{1}{6z_{e_r}^k}} \frac{\partial z_{e_r}^k}{\partial \rho_e} \Delta\gamma_{e_r}^k \\ \frac{1}{2} \hat{\boldsymbol{\sigma}}_{e_r}^{k^T} \frac{\partial \boldsymbol{P}}{\partial \rho_e} + \frac{\partial \boldsymbol{q}^T}{\partial \rho_e} \hat{\boldsymbol{\sigma}}_{e_r}^k - 2\zeta \frac{\partial \zeta}{\partial \rho_e} \end{bmatrix} \tag{72}$$

The derivatives $\partial \hat{\boldsymbol{C}}^e / \partial \rho_e$, $\partial \boldsymbol{P} / \partial \rho_e$, $\partial \boldsymbol{q} / \partial \rho_e$, $\partial z_{e_r}^k / \partial \rho_e$ and $\partial \zeta / \partial \rho_e$ come from the material interpolation.

Appendix B: Sensitivity verification

The sensitivity analysis outlined in Section 3.3 is verified in this Appendix by comparing the values computed using the analytical adjoint method with those obtained numerically using the central difference method (CDM). The CDM calculates the sensitivity of a response function F with respect to a design variable x_e as

$$\frac{\partial F(\boldsymbol{x})}{\partial x_e} \approx \frac{F(\boldsymbol{x} + \Delta \boldsymbol{h}) - F(\boldsymbol{x} - \Delta \boldsymbol{h})}{2\Delta h} \tag{73}$$

where $\boldsymbol{x}$ is the full vector of design variables and $\Delta \boldsymbol{h}$ is a vector with entries of zero except at the index corresponding to x_e, where the entry is the perturbation value Δh.

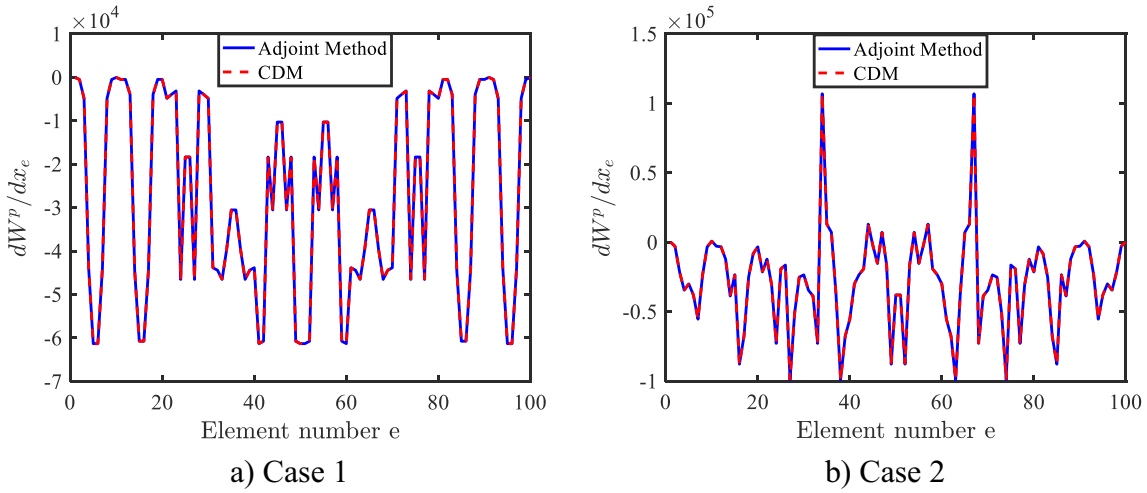

Fig. 16 Comparison of sensitivity values obtained using the adjoint method and CDM with $\Delta h = 10^{-5}$ for two cases of Hoffman plasticity under simple shear

The perturbation value for CDM used in the following verification study is $\Delta h = 10^{-5}$.

The example used for sensitivity verification is a square RUC domain discretized into a 10×10 mesh of plane strain Q1/E4 EAS elements with a thickness of 1. The discretized domain and element numbering are shown in Fig. 15a. The size of the domain is set to 1000 by 1000 and the elastic material parameters are $E = 2500$ and $\nu = 0.38$. The hardening coefficient $K^h = 125$ and is normalized by the yield stress $\sigma_y = 20$.

The density distribution used for this example is shown in Fig. 15b, where the density values within the square inclusion are $\rho_{in} = 0.2$ while the outer density values are $\rho_{out} = 0.7$. The penalization parameters p_0 and p_1 are set to 3 and 2.5, respectively. No filter is utilized so that in this case $\partial F/\partial \boldsymbol{x} = \partial F/\partial \boldsymbol{\rho}$. The RUC is subject to a simple shear deformation by prescribing the macroscopic strain tensor as $\hat{\bar{\boldsymbol{\varepsilon}}} = \begin{bmatrix} 0 & 0 & 0.2 \end{bmatrix}$. Two verification cases are run using this example. In case 1, the scaling factors χ and ω are set to 1 and the angle $\theta = 0$, resulting in the von Mises model without rotation. In case 2, $\omega = 4$, $\chi = 2$ and $\theta = \pi/4$. Figure 16 shows the sensitivity values calculated using the two cases of material parameters. From here it can be seen that the sensitivity values match closely, verifying the correct implementation of the path-dependent adjoint sensitivity analysis from Section 3.3.

References

Alberdi R, Khandelwal K (2017) Topology optimization of pressure dependent elastoplastic energy absorbing structures with material damage constraints. Finite Elem Anal Des 133:42–61. https://doi.org/10.1016/j.finel.2017.05.004

Alberdi R, Zhang G, Khandelwal K (2018a) A framework for implementation of rve-based multiscale models in computational homogenization using isogeometric analysis. Int J Numer Methods Eng 114(9):1018–1051. https://doi.org/10.1002/nme.5775

Alberdi R, Zhang G, Li L, Khandelwal K (2018b) A unified framework for nonlinear path-dependent sensitivity analysis in topology optimization. International Journal for Numerical Methods in Engineering. https://doi.org/10.1002/nme.5794

Amstutz S, Andra H (2006) A new algorithm for topology optimization using a level-set method. J Comput Phys 216(2):573–588. https://doi.org/10.1016/j.jcp.2005.12.015

Amstutz S, Giusti SM, Novotny AA, de Souza Neto EA (2010) Topological derivative for multi-scale linear elasticity models applied to the synthesis of microstructures. Int J Numer Methods Eng 84(6):733–756. https://doi.org/10.1002/nme.2922

Aymeric M, Allaire G, Jouve F (2018) Elasto-plastic shape optimization using the level set method. SIAM J Control Optim 56(1):556–581. https://doi.org/10.1137/17M1128940

Bendsøe MP, Sigmund O (1999) Material interpolation schemes in topology optimization. Arch Appl Mech 69(9):635–654. https://doi.org/10.1007/s004190050248

Bendsøe MP, Sigmund O (2003) Topology optimization: theory, methods and applications, 2nd edn. Springer Science & Business Media, Berlin

Bensoussan A, Lions JL, Papanikolau G (1978) Asymptotic analysis for periodic structures. North Holland, Amsterdam

Blanco PJ, Sánchez PJ, de Souza Neto EA, Feijóo RA (2016) Variational foundations and generalized unified theory of rve-based multiscale models. Arch Comput Meth Eng 23(2):191–253. https://doi.org/10.1007/s11831-014-9137-5

Cadman JE, Zhou S, Chen Y, Li Q (2013) On design of multi-functional microstructural materials. J Mater Sci 48(1):51–66. https://doi.org/10.1007/s10853-012-6643-4

Cantrell J, Rohde S, Damiani D, Gurnani R, DiSandro L, Anton J, Young A, Jerez A, Steinbach D, Kroese C, Ifju P (2017) Experimental characterization of the mechanical properties of 3d printed abs and polycarbonate parts. In: Yoshida S, Lamberti L, Sciammarella C (eds) Advancement of optical methods in experimental mechanics, vol 3. Springer International Publishing, Cham, pp 89–105

Carstensen JV, Lotfi R, Guest JK, Chen W, Schroers J (2015) Topology optimization of cellular materials with maximized energy absorption. International Design Engineering Technical Conferences and Computers and Information in Engineering Conference Volume 2B: 41st Design Automation Conference. https://doi.org/10.1115/DETC2015-47757

Chen W, Xia L, Yang J, Huang X (2018) Optimal microstructures of elastoplastic cellular materials under various macroscopic strains. Mech Mater 118:120–132. https://doi.org/10.1016/j.mechmat.2017.10.002

Christensen J, Kadic M, Kraft O, Wegener M (2015) Vibrant times for mechanical metamaterials. MRS Commun 5(3):453–462. https://doi.org/10.1557/mrc.2015.51

Crisfield M (1991) Non-linear finite element analysis of solids and structures. Wiley, West Sussex

De Borst R, Feenstra PH (1990) Studies in anisotropic plasticity with reference to the hill criterion. Int J Numer Methods Eng 29(2):315–336. https://doi.org/10.1002/nme.1620290208

De Souza Neto EA, Feijoo RA (2006) Variational foundations of multi-scale constitutive models of solid: small and large strain kinematical formulation. LNCC Research & Development Report 16

De Souza Neto EA, Amstutz S, Giusti SM, Novotny AA (2010) Topological derivative-based optimization of micro-structures considering different multi-scale models. CMES: Comput Model Eng Sci 62(1):23–56. https://doi.org/10.3970/cmes.2010.062.023

De Souza Neto EA, Peric D, Owen DRJ (2011) Computational methods for plasticity: theory and applications. Wiley, West Sussex

Deaton JD, Grandhi RV (2014) A survey of structural and multidisciplinary continuum topology optimization: post 2000. Struct Multidiscip Optim 49(1):1–38. https://doi.org/10.1007/s00158-013-0956-z

Fleck NA, Deshpande VS, Ashby MF (2010) Micro-architectured materials: past, present and future. Proc R Soc London Math Phys Eng Sci 466(2121):2495–2516. https://doi.org/10.1098/rspa.2010.0215

Frazier WE (2014) Metal additive manufacturing: a review. J Mater Eng Perform 23(6):1917–1928. https://doi.org/10.1007/s11665-014-0958-z

Geers M, Kouznetsova V, Brekelmans W (2010) Multi-scale computational homogenization: trends and challenges. J Comput Appl Math 234(7):2175–2182. https://doi.org/10.1016/j.cam.2009.08.077

Gibiansky LV, Sigmund O (2000) Multiphase composites with extremal bulk modulus. J Mech Phys Solids 48(3):461–498. https://doi.org/10.1016/S0022-5096(99)00043-5

Giusti S, Novotny A, de Souza Neto E, Feijoo R (2009) Sensitivity of the macroscopic elasticity tensor to topological microstructural changes. J Mech Phys Solids 57(3):555–570. https://doi.org/10.1016/j.jmps.2008.11.008

Guo N, Leu MC (2013) Additive manufacturing: technology, applications and research needs. Front Mech Eng 8(3):215–243. https://doi.org/10.1007/s11465-013-0248-8

Hill R (1948) A theory of the yielding and plastic flow of anisotropic metals. Proc R Soc London Math Phys Eng Sci 193(1033):281–297. https://doi.org/10.1098/rspa.1948.0045

Hill R (1963) Elastic properties of reinforced solids: Some theoretical principles. J Mech Phys Solids 11(5):357–372. https://doi.org/10.1016/0022-5096(63)90036-X

Hill R (1967) The essential structure of constitutive laws for metal composites and polycrystals. J Mech Phys Solids 15(2):79–95. https://doi.org/10.1016/0022-5096(67)90018-X

Kasper EP, Taylor RL (1997) A mixed enhanced strain method: Linear problems. Department of Civil and Environmental Engineering, University of California at Berkeley; Report No: UCB/SEMM-97/02

Kasper EP, Taylor RL (2000) A mixed-enhanced strain method: Part i: Geometrically linear problems. Comput Struct 75(3):237–250. https://doi.org/10.1016/S0045-7949(99)00134-0

Kato J, Hoshiba H, Takase S, Terada K, Kyoya T (2015) Analytical sensitivity in topology optimization for elastoplastic composites. Struct Multidiscip Optim 52(3):507–526. https://doi.org/10.1007/s00158-015-1246-8

Lee JH, Singer JP, Thomas EL (2012) Micro-/nanostructured mechanical metamaterials. Adv Mater 24(36):4782–4810. https://doi.org/10.1002/adma.201201644

Lefebvre LP, Banhart J, Dunand DC (2008) Porous metals and metallic foams: Current status and recent developments. Adv Eng Mater 10(9):769–774. https://doi.org/10.1002/adem.200890025

Li J, Wu B, Myant C (2016) The current landscape for additive manufacturing research. ICL AMN report

Li L, Zhang G, Khandelwal K (2017a) Topology optimization of energy absorbing structures with maximum damage constraint. Int J Numer Methods Eng 112(7):737–775. https://doi.org/10.1002/nme.5531

Li L, Zhang G, Khandelwal K (2017b) Topology optimization of energy absorbing structures with maximum damage constraint. Int J Numer Methods Eng 112(7):737–775. https://doi.org/10.1002/nme.5531

Mandel J (1966) Contribution theorique a l'etude de l'ecrouissage et des lois de l'ecoulement plastique. Springer, Berlin

Maute K, Schwarz S, Ramm E (1998) Adaptive topology optimization of elastoplastic structures. Struct Optim 15(2):81–91. https://doi.org/10.1007/BF01278493

Miehe C, Koch A (2002) Computational micro-to-macro transitions of discretized microstructures undergoing small strains. Arch Appl Mech 72(4):300–317. https://doi.org/10.1007/s00419-002-0212-2

Neves M, Rodrigues H, Guedes J (2000) Optimal design of periodic linear elastic microstructures. Comput Struct 76(1):421–429. https://doi.org/10.1016/S0045-7949(99)00172-8

Osanov M, Guest JK (2016) Topology optimization for architected materials design. Annu Rev Mater Res 46(1):211–233. https://doi.org/10.1146/annurev-matsci-070115-031826

Pavliotis G, Stuart A (2008) Multiscale methods: averaging and homogenization. Springer-Verlag, New York

Rashed M, Ashraf M, Mines R, Hazell PJ (2016) Metallic microlattice materials: A current state of the art on manufacturing, mechanical properties and applications. Mater Des 95:518–533. https://doi.org/10.1016/j.matdes.2016.01.146

Saeb S, Steinmann P, Javili A (2016) Aspects of computational homogenization at finite deformations: a unifying review from reuss' to voigt's bound. Appl Mech Rev 68(5):050801-33. https://doi.org/10.1115/1.4034024

Schaedler TA, Ro CJ, Sorensen AE, Eckel Z, Yang SS, Carter WB, Jacobsen AJ (2014) Designing metallic microlattices for energy absorber applications. Adv Eng Mater 16(3):276–283. https://doi.org/10.1002/adem.201300206

Schellekens J, De Borst R (1990) The use of the hoffman yield criterion in finite element analysis of anisotropic composites. Comput Struct 37(6):1087–1096. https://doi.org/10.1016/0045-7949(90)90020-3

Sigmund O (1994) Materials with prescribed constitutive parameters: An inverse homogenization problem. Int J Solids Struct 31(17):2313–2329. https://doi.org/10.1016/0020-7683(94)90154-6

Sigmund O (1995) Tailoring materials with prescribed elastic properties. Mech Mater 20(4):351–368. https://doi.org/10.1016/0167-6636(94)00069-7

Sigmund O (2000) A new class of extremal composites. J Mech Phys Solids 48(2):397–428. https://doi.org/10.1016/S0022-5096(99)00034-4

Simo JC, Rifai MS (1990) A class of mixed assumed strain methods and the method of incompatible modes. Int J Numer Methods Eng 29(8):1595–1638. https://doi.org/10.1002/nme.1620290802

Strang G (2007) Computational science and engineering. Wellesley-Cambridge Press, Wellesley

Svanberg K (1987) The method of moving asymptotes—a new method for structural optimization. Int J Numer Methods Eng 24(2):359–373. https://doi.org/10.1002/nme.1620240207

Swan CC, Arora JS (1997) Topology design of material layout in structured composites of high stiffness and strength. Struct Optim 13(1):45–59. https://doi.org/10.1007/BF01198375

van Dijk NP, Maute K, Langelaar M, van Keulen F (2013) Level-set methods for structural topology optimization: a review. Struct Multidiscip Optim 48(3):437–472. https://doi.org/10.1007/s00158-013-0912-y

Xu Q, Lv Y, Dong C, Sreeprased TS, Tian A, Zhang H, Tang Y, Yu Z, Li N (2015) Three-dimensional micro/nanoscale architectures: fabrication and applications. Nanoscale 7:10883–10895. https://doi.org/10.1039/C5NR02048D

Zhang G, Li L, Khandelwal K (2017) Topology optimization of structures with anisotropic plastic materials using enhanced assumed strain elements. Struct Multidiscip Optim 55(6):1965–1988. https://doi.org/10.1007/s00158-016-1612-1